



Assessing advantages and disadvantages of macro- and micro-channel flow boiling for high-heat-flux thermal management using computational and theoretical/empirical methods

V.S. Devahdhanush^{a,1}, Yuchuan Lei^{b,1}, Zhenqian Chen^b, Issam Mudawar^{a,*}

^a Purdue University Boiling and Two-Phase Flow Laboratory (PU-BTFFL), School of Mechanical Engineering, Purdue University, 585 Purdue Mall, West Lafayette, IN 47907, USA

^b School of Energy & Environment, Southeast University, Nanjing, Jiangsu, PR China

ARTICLE INFO

Article history:

Received 10 September 2020

Revised 12 November 2020

Accepted 29 November 2020

Available online 19 January 2021

Keywords:

flow boiling

micro-channel

macro-channel

choking

CFD

two-phase heat sinks

ABSTRACT

This study examines the advantages and disadvantages of micro- and macro-channel flow boiling for high-heat-flux cooling applications using both computational and theoretical/empirical methods. The computational simulations are conducted in ANSYS FLUENT using the Volume of Fluid (VOF) method along with the Lee phase change model, and accounting for both shear lift force and conjugate heat transfer along the channel walls. Computational results for both channel sizes are compared with theoretical/empirical results obtained using the Homogeneous Equilibrium Model (HEM) and Separated Flow Model (SFM), and both HEM and the Homogenous Frozen Model (HFM) are used to assess the potential for two-phase choking. The computational results show bubbles in micro-channels are highly confined and tend to grow longer in the flow direction. The two methods show good agreement in predicting wall temperatures. Overall, micro-channel heat sinks are shown to fare much better than macro-channels in terms of heat transfer performance, evidenced by both significantly higher heat transfer coefficients and lower wall temperatures, but this comes at the cost of significantly higher pressure drop and pumping power requirements. It is also shown micro-channels are prone to choking due to high two-phase Mach number.

© 2020 Elsevier Ltd. All rights reserved.

1. Introduction

1.1. Implementation of Macro-channel and Micro-channel Flow Boiling in Modern High-Heat-Flux Applications

Recent advances in many modern applications have increased functionality while decreasing size and weight of electronic and power devices, causing appreciable and monotonic increases in heat dissipation and therefore demanding more effective heat removal technologies. Examples include computer data centers, hybrid vehicle power electronics, x-ray medical devices, aircraft and spacecraft avionics, advanced radar, and laser and microwave electronics [1–4]. Effective cooling requires that devices be maintained within safe operating temperature limits, which is essential to improving device speed and reliability as well to increasing lifespan.

The increased heat dissipation in high performance devices has made obsolete all air cooling and most single-phase liquid cooling technologies, and shifted interest to two-phase cooling schemes, which are better able to tackle high heat flux situations by capitalizing on both sensible and latent heat of the coolant.

A two-phase thermal management system utilizes a two-phase fluid conditioning loop, wherein the heat from high heat flux devices is removed by boiling and rejected to the ambient with the aid of condenser. Developing both a fundamental understanding and practical implementation of boiling as an effective means for the heat removal has been a primary research focus for the Purdue University Boiling and Two-Phase Flow Laboratory (PU-BTFFL) dating back to 1984. Studies at PU-BTFFL have encompassed virtually all boiling schemes, including capillary [5], pool boiling [6,7], falling film [8], macro-channel flow boiling [9], micro-channel flow boiling [10,11], jet-impingement [12], spray [13], and combinations thereof [14].

Several important lessons have been learned from these efforts [1]. First, capillary solutions (such as heat pipes, capillary pumped loops, and loop heat pipes), which rely on surface tension to trans-

* Corresponding author.

E-mail address: mudawar@ecn.purdue.edu (I. Mudawar).

URL: <https://engineering.purdue.edu/BTFFL> (I. Mudawar)

¹ Equal contribution as joint first authors (listed alphabetically).

Nomenclature

A_c	channel cross-sectional area
Bo	boiling number, q''_w/Gh_{fg}
C	parameter in empirical correlations
c_p	specific heat at constant pressure
ΔC	computational grid size
D_h	hydraulic diameter
E	specific internal energy (energy per unit mass)
F_σ	surface tension force
f	friction factor
f_{app}	apparent friction factor
G	mass velocity
g	gravitational acceleration
h	enthalpy; heat transfer coefficient
h_{fg}	latent heat of vaporization
I	turbulent intensity
Ja^*	modified Jacob number, $c_{p,f}\Delta T_{sub,in}/h_{fg}$
k	thermal conductivity; turbulence kinetic energy
L	channel length
M	two-phase Mach number
\dot{m}	total mass flow rate for heat sink
N	number of channels in heat sink
Nu	Nusselt number
P	pressure
ΔP	pressure drop
P_{crit}	critical pressure of fluid
P_F	frictional perimeter of channel
P_H	heated perimeter of channel
Pr	Prandtl number
P_R	reduced pressure, P/P_{crit}
Q	energy source term
Q_v	total volumetric flow rate for heat sink
q''_b	base heat flux based on heated area of heat sink
q''_w	wall heat flux based on heated area of channel
Re	Reynolds number
S	mass source term
Su	Suratman number
T	temperature
ΔT_{sub}	fluid subcooling, $T_{sat} - T_f$
t	computational time
u	velocity; bulk fluid velocity
u'	root-mean-square of turbulent velocity fluctuation
\bar{u}	mean velocity
u_τ	friction velocity
v	specific volume
w	transverse pitch of channels in heat sink
W	width of heat sink
We	Weber number
X	Lockhart-Martinelli parameter
x	vapor quality
x_e	thermodynamic equilibrium quality, $(h - h_f)/h_{fg}$
y	coordinate perpendicular to wall
z	streamwise coordinate

Greek symbols

α	volume fraction; void fraction
β	channel aspect ratio for rectangular channels
γ	mass transfer intensity factor
δ^+	dimensionless thickness of hydrodynamic boundary layer
ε	turbulence dissipation rate
θ	channel inclination with horizontal
μ	dynamic viscosity

ν	kinematic viscosity
ρ	density
σ	surface tension
τ	shear stress
ϕ	two-phase pressure drop multiplier
ω	turbulence specific dissipation rate; parameter in Beattie and Whalley two-phase mixture viscosity model

Subscripts

A	accelerational
ad	adiabatic
c	critical
cb	convective boiling
F	frictional
f	saturated liquid; single-phase liquid; bulk fluid
fo	liquid only
g	saturated vapor; single-phase vapor
go	vapor only
in	channel inlet
k	index for a phase: liquid (f) or vapor (g)
lam	fully developed laminar
micro	micro-channel
macro	macro-channel
nb	nucleate boiling
out	channel outlet
sat	saturated
sb	saturated boiling
sc	subcooled boiling
sp	single-phase
t	turbulent
tot	total
tp	two-phase
$turb$	fully developed turbulent
v	laminar
w	channel wall
z	local

port the coolant, are effective only for low-range heat fluxes (well below 100 W/cm^2) and therefore not suitable for high flux situations. Second, pool boiling, which relies on buoyancy to circulate the coolant in a thermosyphon, performs better than capillary systems, but is limited to midrange heat fluxes. Third, using a pump to increase coolant flow rate is essential to improving cooling performance. This is true for macro- and micro-channel, jet-impingement and spray cooling schemes, evidenced by their ability to remove much higher heat fluxes than those relying on capillarity or buoyancy. A detailed assessment of both the merits and disadvantages of each of the pumped systems is available in [2]. The present study is focused entirely on the first two, macro- and micro-channel flow boiling.

As discussed in [15], use of small channels to improve cooling performance dates back to the 1970s, and includes cooling of both industrial turbine blades and electrode walls of magneto-hydrodynamic (MHD) energy conversion systems. Several criteria have been proposed to demarcate macro- and micro-channels (e.g., [16,17]), but there is no clear consensus on which criterion to use. Typically, micro-channels of practical interest possess diameters in the range of $0.1 - 0.6 \text{ mm}$ [2].

As discussed in [15], many recent studies provide strong evidence that micro-channel flow boiling can provide cooling performance superior to that of macro-channels. Micro-channel devices are also far more compact and lightweight, two attributes highly sought after in modern cooling applications. But superior heat transfer performance for micro-channels comes at the cost

of much higher pressure drop, as well as a host of possible operational anomalies stemming from large changes in the coolant's thermophysical properties, let alone increased likelihood of flow instabilities.

1.2. Predictive Methods for Two-Phase Channel Flow and Heat Transfer

1.2.1. Empirical and Semi-empirical Methods

Empirical and semi-empirical correlations remain the most widely used approaches to predicting two-phase flow and heat transfer in channels. A key weakness of most is that they tend to be developed for one or a few fluids and are applicable to specific flow patterns as well as narrow ranges of geometrical parameters and operating conditions. But a new class of highly improved correlations has emerged which provides broad coverage of many fluids and most relevant parameters (e.g., [18–23] for pressure drop and [24–26] for heat transfer). Constructing such correlations relies heavily on acquisition of massive database from World literature. Coining the phrase “universal correlations”, Kim and Mudawar provided ample evidence of the effectiveness and predictive accuracy of correlations derived from massive databases for pressure drop [27] and two-phase heat transfer coefficient [28,29]. However, despite their many advantages, such correlations cannot predict details of interfacial behavior or flow patterns along the channel.

1.2.2. Theoretical Models

Theoretical models constitute another important approach to predicting two-phase flow and heat transfer in channels. Given the appeal of flow separation between phases in annular flow, the vast majority of these models is derived specifically for this flow pattern. Here, pressure drop and heat transfer coefficient (for both flow boiling and flow condensation) are calculated by applying conservation laws to the vapor core and annular film separately, and matching velocities, temperatures, and mass transfer rates along the film's interface. Detailed discussions regarding these models are available in [30,31]. Overall, the main drawback of theoretical models is focus on a single flow pattern, and therefore inability to tackle other patterns of interest.

1.2.3. Computational Models

The advent of powerful computational fluid mechanics tools has recently created an enormous opportunity to model complex multi-phase flows. Computational Fluid Dynamics (CFD) tools help in the simulation of spatial and temporal distributions of flow and thermal features, which is not possible with other predictive methods. This helps explain the great attention being paid to the use of CFD for both design and performance prediction of thermal systems. But, while CFD tools have shown great success in simulating single-phase flows, they have been less effective in modeling two-phase flows both because of inherent inaccuracies in the submodels used and reliance on powerful (and often expensive) computational resources. And, even with the availability of such resources, a single simulation might sometimes require many weeks to execute. Clearly, this hinders the utility of CFD as a viable and robust tool for simulating two-phase flows. More work is therefore needed to improve CFD methods and make them computationally more efficient.

An important step when using CFD to tackle two-phase situations is capturing the liquid-vapor interface with sufficient accuracy and accurately tackling the transport boundary conditions along the interface. Of the different CFD methods presently available, the Euler-Lagrange and the Euler-Euler approaches have achieved most success in modeling rather complex phase-change configurations because of their ability to track the individual phases and the interactions between them [32]. The Euler-Lagrange

approach provides more accurate predictions because of its higher interface tracking accuracy and ease of applying interfacial boundary conditions. However, it is computationally very demanding and suffers poor convergence. The Euler-Euler approach is simpler to use and treats the two phases as interpenetrating continua and defines volume fraction for each phase as a continuous function of both space and time. The Euler-Euler approach can be implemented using the Volume of Fluid (VOF) model, the Mixture model, or the Eulerian model [32].

The VOF method is the most popular of the Euler-Euler methods and has been adopted in many recent flow boiling simulations (e.g., [33–37]) because of its inherent conservativeness, stability, reasonable efficiency, and ease of implementation. The VOF method tracks a moving interface by the volume fraction of each phase in each computational cell, which is then used to implicitly construct the liquid-vapor interface. The accuracy of the interface topography prediction can be improved by applying an interface reconstruction scheme such as Piecewise Linear Interface Calculation (PLIC) [38]. Other efforts to improve the accuracy of interface tracking in flow boiling are discussed in refs. [39–41].

Three popular phase change (mass transfer) models are primarily used in the literature: Sharp Interface model, Schrage model, and Lee model [32]. The Sharp Interface model assumes that interfacial phase change is the sole cause of heat transfer, and is based on the Rankine-Hugoniot jump condition [42] for energy conservation. Schrage [43] analyzed liquid-vapor interfacial mass transfer using Maxwellian distribution kinetic theory, and applied the Hertz-Knudsen equation to tackle the temperature and pressure jumps at the interface. The Lee model [44] is a derivative of Schrage's model but formatted to overcome inherent disadvantages of the latter. In the Lee model, evaporative phase change can occur both at the liquid-vapor interface and in the saturated liquid phase. There have been many attempts to improve each of these models (e.g., [41,45–50]).

1.3. Previous Computational Simulations of Flow Boiling in Channels

1.3.1. CFD Models of Macro-channels

Table 1 provides a summary of prior computational work on flow boiling in macro-channels. One of the main objectives for several of these studies is determining shape, size, velocity, and trajectory of bubbles in subcooled flow boiling [33,35,51]. Bahreini *et al.* [52] examined subcooled boiling flow patterns, heat transfer, and pressure drop under both microgravity and normal gravity. And Vadlamudi and Nayak [53] used CFD to predict Departure from Nucleate Boiling (DNB). Recently, Lee *et al.* [54] proposed a 2D CFD model to predict subcooled flow boiling in a rectangular channel and provided detailed predictions of bubble generation, coalescence, detachment, and deformation, as well as both axial and transverse distributions of void fraction, velocity, and temperature. Their follow-up study [55] extended simulations to 3D, which provided more accurate predictions than the 2D model.

1.3.2. CFD Models of Mini/Micro-channels

Table 2 provides a summary of prior computational work on flow boiling in mini/micro-channels. This topic has received noticeable attention in recent years given the importance of micro-channel cooling to many modern applications. Prior work includes simulations of single bubble behavior [34,37,56–58], flow pattern transitions [36,59–67], flow and thermal fields [34,37,58,60–64,66], pressure drop [60,64], heat transfer [34,36,56–59,61,62,65,66], and critical heat flux (CHF) [66]. They also include investigations into effects of operating conditions [36,56,57,59,60,63–67], forces [36,59], channel geometry [36,56,57,59], flow orientation [66], wall surface conditions [63,66], contact angle [56–58], Marangoni heat transfer [36], and fluid properties [67] on both bubble behavior

Table 1
Summary of previous computational simulations of flow boiling in macro-channels.

Author(s)	Fluid	Computational domain ^a	Operating conditions	Method	Comments
Jeon et al. [33] (2011)		V, S, 3D $D_h = 15$ mm $L = 800$ mm		VOF, bubble condensation model	Condensing bubble behavior including velocity and trajectory
Pan et al. [51] (2012)	water	V, R, 3D $D_h = 2.857, 15$ mm $L = 10, 30$ mm	$G = 300\text{--}500$ kg/m ² s $\Delta T_{sub} = 5\text{--}40^\circ\text{C}$ $P_{in} = 1\text{--}4$ bar	VOF, mass and heat transfer model	Bubble size and deformation; flow field characteristics
Bahreini et al. [35] (2015)	water	V, 2D $D_h = 10$ mm $L = 20$ mm	$G = 0\text{--}296$ kg/m ² s $T_{in} = 100^\circ\text{C}$ $T_w = 70\text{--}95^\circ\text{C}$	VOF, CSF, Lee model ($\gamma = 100$ s ⁻¹)	Effects of velocity, bubble size and temperature gradient on bubble behavior
Vadlamudra & Nayak [53] (2017)	water	V, SP, 2D $D_h = 7.7\text{--}11$ mm $L = 457.2$ mm	$G = 1351\text{--}2715$ kg/m ² s $T_{sat} = 148.15\text{--}227.55^\circ\text{C}$ $P_{in} = 138$ MPa $q''_w = 3000\text{--}5360$ kW/m ²	Eulerian, wall boiling model, $k\text{--}\epsilon$	Impact of different parameters on DNB
Bahreini et al. [52] (2017)	HFE-7100	H, SP, C, 2D $D_h = 6$ mm $L = 200$ mm	$G = 20\text{--}210$ kg/m ² s $q''_w = 20\text{--}160$ kW/m ² $T_{sat} = 54^\circ\text{C}$	CFVOF, CSF, Lee model ($\gamma = 1$ s ⁻¹)	Effects of heat flux and mass velocity on flow patterns and heat transfer coefficient in microgravity and normal gravity
Hasanpour et al. [102] (2018)	water	V, SP, 2D $D_h = 2.54\text{--}5.08$ mm $L = 280$ mm	$G = 151$ kg/m ² s $T_{sat} = 80^\circ\text{C}$ $q''_w = 182$ kW/m ²	VOF, CSF, $k\text{--}\omega$ SST, Lee model ($\gamma = 10$ s ⁻¹)	Oscillatory flow features and temporal variations of vapor void fraction
Lee et al. [54] (2019)	FC-72	V, SP, R, 3D $D_h = 5$ mm $L = 144.6$ mm	$G = 445.8\text{--}2432.8$ kg/m ² s $T_{sat} = 27.82\text{--}35.87^\circ\text{C}$ $q''_w = 146.301\text{--}194.873$ kW/m ²	VOF, CSF, $k\text{--}\omega$ SST, Lee model ($\gamma = 10$ s ⁻¹)	Flow patterns, axial and transverse distributions of void fraction, velocity and temperature; axial variations of wall temperature and heat transfer coefficient
Dong et al. [41] (2019)	water	H, SP, R, 3D $D_h = 17.68$ mm $L = 500$ mm	$G = 193\text{--}968$ kg/m ² s $T_{in} = 85\text{--}95^\circ\text{C}$ $q''_w = 126\text{--}462$ kW/m ²	VOF, CSF, $k\text{--}\omega$ SST, Lee model	Employs an interphase mass transfer model based on the Lee model
Yin et al. [77] (2019)	water	H, SP, R, 3D $D_h = 50$ mm $L = 5000$ mm	$T_{in} = 110^\circ\text{C}$ $q''_w = 11.8$ kW/m ²	VOF, CSF, Realizable $k\text{--}\epsilon$, Lee model ($\gamma = 0.1$ s ⁻¹)	Bubble motion; two-phase flow regimes; local heat transfer characteristics
Lee et al. [55] (2020)	FC-72	V, SP, R, 3D $D_h = 3.33$ mm $L = 129.6$ mm	$G = 176.96\text{--}2438.28$ kg/m ² s $T_{in} = 20\text{--}26^\circ\text{C}$ $P_{in} = 0.113\text{--}0.151$ MPa $q''_w = 0.104\text{--}0.194$ kW/m ²	VOF, CSF, $k\text{--}\omega$ SST, Lee model ($\gamma_g = 0.1$ s ⁻¹ , $\gamma_f = 100$ s ⁻¹), Shear-lift model	Effects of shear-lift force on bubble motion; fluid flow and heat transfer characteristics; velocity and temperature profiles

^a H: horizontal, V: vertical, SP: single port, C: circular, R: rectangular, S: square

and heat transfer characteristics. Some studies show that as vapor bubbles nucleate and grow, they leave behind a thin liquid film at the wall [34,58,61]; they also attribute improved heat transfer in small channels to evaporation of the liquid film. It must be noted that most CFD studies have been dedicated to single bubble behavior rather than capturing the entire fluid flow and heat transfer characteristics for a multitude of bubbles along the flow channel.

1.4. Objectives of Study

One problem that is of paramount importance to modern high-heat-flux applications is choosing hydraulic diameter for a multi-channel heat sink that would provide best overall performance, including pressure drop, heat transfer, and flow stability. This is precisely the goal of the present study. Considered in this study, as shown in Fig. 1, is a square heat sink having a practical size of 25 mm x 25 mm ($W \times L$), which is subjected on its underside to a uniform base heat flux q''_b . Coolant FC-72 flows through a number of parallel horizontal channels of diameter D_h and transverse pitch w , and all other walls are perfectly insulated. The key question regarding the heat sink performance is how does D_h affect overall performance, subject to the constraints of fixed outlet pressure, P_{out} , inlet fluid temperature, T_{in} , and mass flow rate, \dot{m} , as well as fixed total heat transfer area of all channels combined? More specifically, is a micro-channel preferred over a macro-channel or vice versa?

To answer these important questions, two different predictive methods will be used: (i) CFD simulation and (ii) theoretical/empirical approach. Use of the two different methods is intended to validate consistency of predictions. Both methods are used to predict fluid flow, pressure drop, and heat transfer characteristics for different mass flow rates and base heat fluxes in heat sinks with two channel diameters: 0.5 mm (representing micro-channels) and 5 mm (representing macro-channels). Also assessed by analytic models is the likelihood of two-phase choking in both channels. This study further gives details of systematic predictions of both predictive methods and demonstrates their capabilities in assessing the advantages and disadvantages of micro- and macro-channels without experimentation.

2. Computational Methods

2.1. Geometrical Parameters and Operating Conditions

The geometrical parameters and operating conditions for the different FC-72 cases considered in the present study are listed in Table 3, where N , q''_b , q''_w , Q_v , G , and T_{in} , are, respectively, number of channels, heat flux along the base of the heat sink, heat flux along inner walls of channels, total flow rate, mass velocity, and inlet temperature. Table 3 also includes values for thermodynamic equilibrium quality at both the inlet, $x_{e,in}$, and outlet, $x_{e,out}$, corresponding to a fixed outlet pressure of $P_{out} = 120$ kPa. The $x_{e,in}$ and

Table 2
Summary of previous computational simulations of flow boiling in mini/micro-channels.

Author(s)	Fluid(s)	Computational domain ^b	Operating conditions	Method	Comments
Lee & Son [56] (2008)	water	H, SP, R, 3D $D_h = 0.2\text{-}3.33$ mm $L = 10\text{-}22.5$ mm	$G = 118.4$ kg/m ² s $T_{in} = 100^\circ\text{C}$ $P_{in} = 1$ bar $T_w = 105\text{-}120^\circ\text{C}$	LSVOF, CSF, Son <i>et al.</i> [103] phase change model	Effects of contact angle on liquid layer, bubble growth rate and heat transfer; effects of channel size on bubble growth rate and heat transfer
Suh <i>et al.</i> [57] (2008)	water	H, SP, R, 3D $D_h = 0.266$ mm $L = 10$ mm	$G = 98.7$ kg/m ² s $T_{in} = 100^\circ\text{C}$ $P_{in} = 1$ bar $T_w = 105^\circ\text{C}$	LSVOF, CSF, Son <i>et al.</i> [103] phase change model	Effects of contact angle, wall superheat, and number of channels on bubble growth, flow reversal, and heat transfer
Mukherjee [58] (2009)	water	H, SP, S, 3D $D_h = 0.2$ mm	$G = 144.1$ kg/m ² s $T_w = 108^\circ\text{C}$ $T_{sat} = 100^\circ\text{C}$	LSVOF	Flow and temperature fields and heat transfer near contact region of liquid-vapor interface for pool boiling, evaporation of a moving meniscus, and flow boiling in a micro-channel
Zhuan & Wang [36] (2010)	water	H, SP/MP, S, 3D $D_h = 0.041, 0.38$ mm $L = 25.4$ mm	$G = 341$ kg/m ² s $T_{in} = 106^\circ\text{C}$ $q''_w = 161.6\text{-}255$ kW/m ²	VOF, CSF, heat and mass transfer model	Examined Marangoni heat transfer, bubble behavior, and flow stability
Wei <i>et al.</i> [60] (2011)	water	V, SP, R, 3D $D_h = 2.857$ mm $L = 20$ mm	$G = 320$ kg/m ² s $q''_w = 200\text{-}500$ kW/m ² $T_{in} = 90^\circ\text{C}$	VOF, CSF, Lee model ($\gamma = 100$ s ⁻¹)	Pressure, velocity and temperature distribution of bubbles; variations of bubble shape
Zhuan & Wang [59] (2011)	HFE-7100	H, SP, R, 3D $D_h = 0.2352$ mm $L = 3.857$ mm	$G = 1000\text{-}3350$ kg/m ² s $q''_w = 60\text{-}400$ kW/m ² $T_{sub,in} = -30, 0^\circ\text{C}$	VOF, CSF, bubble surface heat and mass transfer model	Influence of surface tension on interfacial heat transfer; impact of micro-channel size on onset of nucleate boiling and boiling heat transfer; flow patterns
Zu <i>et al.</i> [37] (2011)	water	H, SP, R, 3D $D_h = 0.606$ mm $L = 40$ mm	$G = 690.9, 747.4$ kg/m ² s $T_w = 115.45^\circ\text{C}$ $T_{sat} = 100^\circ\text{C}$ $q''_w = 210, 220$ kW/m ²	VOF, pseudo-nucleate boiling method, standard $k\text{-}\epsilon$ model	Velocity, temperature and pressure fields; bubble behavior; heat transfer; pressure drop
Zhuan & Wang [67] (2012)	R-134a, R-22	H, SP, C, 3D $D_h = 0.5$ mm $L = 70.7$ mm	$G = 350\text{-}2000$ kg/m ² s $T_{in,sub} = 27^\circ\text{C}$ $q''_w = 50\text{-}129$ kW/m ²	VOF, CSF, phase change model	Bubble growth and coalescence; flow pattern transitions
Magnini <i>et al.</i> [34] (2013)	R113, R145fa, R134a	H, SP, C, 2D $D_h = 0.5$ mm $L = 10\text{-}36$ mm	$G = 500\text{-}600$ kg/m ² s $q''_w = 5\text{-}20$ kW/m ² $T_{sat} = 31, 50^\circ\text{C}$	VOF, CSF, Hardt & Wondra [104] evaporation model	Local bubble behavior, flow and temperature fields; heat transfer model for the film region
Zhou <i>et al.</i> [63] (2013)	water	H, SP, 2D $D_h = 0.107$ mm $L = 40$ mm	$G = 80\text{-}217.14$ kg/m ² s $q''_w = 30\text{-}570$ kW/m ² $T_{in} = 20, 103.05^\circ\text{C}$	LSM, Rayleigh bubble growth model	Bubble behavior; flow boiling regimes; effects of re-entrant cavities; effects of structured surfaces on nucleation and CHF
Magnini <i>et al.</i> [61] (2013)	R113, R145fa	H, SP, C, 2D $D_h = 0.5$ mm $L = 10\text{-}36$ mm	$G = 500\text{-}600$ kg/m ² s $q''_w = 5\text{-}20$ kW/m ² $T_{sat} = 31, 50^\circ\text{C}$	VOF, CSF, Hardt & Wondra [104] evaporation model	Bubble dynamics; flow dynamics within liquid slugs; heat transfer characteristics
Lorenzini & Joshi [64] (2015)	water	V, SP, R, 3D $D_h = 0.2$ mm $L = 5$ mm	$G = 500$ kg/m ² s $q''_w = 0\text{-}270$ kW/m ² $T_{sat} = 60, 100^\circ\text{C}$	VOF, CSF, $k\text{-}\omega$ SST, Lee model ($\gamma = 0.1$ s ⁻¹)	Bubble dynamics; flow and temperature fields; local heat transfer; heat transfer model for film region
Magnini & Thome [62] (2016)	R245fa	H, SP, C, 2D $D_h = 0.51$ mm $L = 15$ mm	$G = 500$ kg/m ² s $q''_w = 0\text{-}20$ kW/m ² $T_{sat} = 31^\circ\text{C}$ $x = 0\text{-}0.02$	VOF, CSF, Hardt & Wondra [104] evaporation model	Bubble length and velocity, liquid film thickness, and liquid slug length in slug flow; heat transfer characteristics
Liu <i>et al.</i> [105] (2017)	R245fa	H, SP, C, 2D $D_h = 0.4$ mm $L = 6$ mm	$G = 400$ kg/m ² s $q''_w = 16080$ kW/m ² $T_{sat} = 31^\circ\text{C}$	CLSVOF, Hardt & Wondra [104] non-equilibrium phase model	Bubble evaporation and growth; flow patterns
Liu <i>et al.</i> [65] (2017)	R134a	V, SP, C, 3D $D_h = 0.64$ mm $L = 5$ mm	$G = 56\text{-}335$ kg/m ² s $q''_w = 5\text{-}15$ kW/m ² $T_{sat} = 27\text{-}30^\circ\text{C}$	CLSVOF, Hardt & Wondra [104] non-equilibrium phase model	Effects of mass velocity and heat flux on bubble growth and flow pattern transitions
Kim & Lee [66] (2019)	water	V, SP, R, 3D $D_h = 0.286$ mm $L = 30$ mm	$G = 20\text{-}500$ kg/m ² s $T_{sat} = 90^\circ\text{C}$ $q''_w = 350$ kW/m ²	Hardt & Wondra [104] non-equilibrium phase model, CSF, Yokoi <i>et al.</i> [106] contact angle model	Bubble nucleation and heat transfer rate on surfaces with different wettability

^b H: horizontal, V: vertical, SP: single port, MP: multi-port, C: circular, R: rectangular, S: square

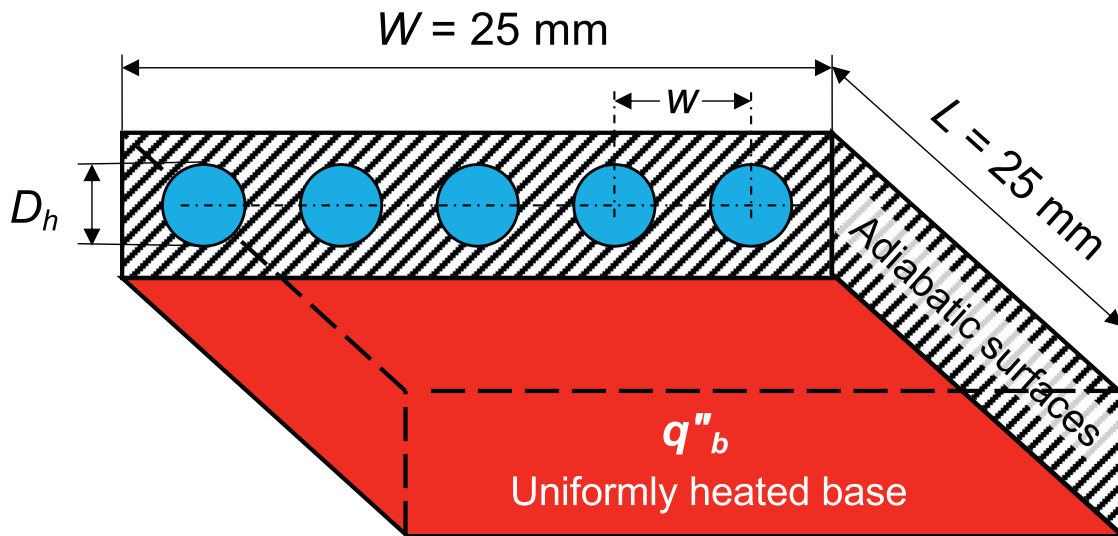


Fig. 1. Schematic of heat sink configuration examined in the present study.

Table 3

Geometrical parameters and operating conditions of micro- and macro-channel heat sinks used in this study. An outlet pressure of $P_{out} = 120$ kPa is used for all cases.

D_h (mm)	w (mm)	N	q''_b (W/cm ²)	q''_w (W/cm ²)	Q_v (mL/min)	G (kg/m ² s)	T_{in} (°C)	$x_{e,in}$ at 120 kPa	$x_{e,out}$ at 120 kPa
0.5	1.25	20	15.08	12	76.59	500	20	-0.4975	0.0180
0.5	1.25	20	30.16	24	76.59	500	20	-0.4975	0.5335
0.5	1.25	20	30.16	24	153.19	1000	20	-0.4975	0.0180
0.5	1.25	20	60.32	48	153.19	1000	20	-0.4975	0.5335
5	12.5	2	15.08	12	76.59	50	20	-0.4975	0.0180
5	12.5	2	30.16	24	76.59	50	20	-0.4975	0.5335
5	12.5	2	30.16	24	153.19	100	20	-0.4975	0.0180
5	12.5	2	60.32	48	153.19	100	20	-0.4975	0.5335

$x_{e,out}$ values shown are used only for guidance regarding the state of fluid at the inlet and outlet when selecting operating conditions.

2.2. Governing Equations

2.2.1. VOF Model

The conditions in Table 3 correspond to subcooled, laminar single-phase liquid flow at the inlet, with vapor transitioning axially from laminar to turbulent.

The transient VOF model is adopted in ANSYS FLUENT [68] and the following assumptions are made:

- (a) Mass is transferred at the interface between the vapor and liquid phases.
- (b) The interface is maintained at saturation temperature of the vapor.
- (c) Gravity effects are neglected.

Tracking of the interface between phases is accomplished by solving continuity equations for volume fraction of each phase.

$$\frac{\partial}{\partial t}(\alpha_f \rho_f) + \nabla \cdot (\alpha_f \rho_f \vec{u}_f) = S_f, \quad (1a)$$

and

$$\frac{\partial}{\partial t}(\alpha_g \rho_g) + \nabla \cdot (\alpha_g \rho_g \vec{u}_g) = S_g, \quad (1b)$$

where S_f and S_g are user-defined mass source terms for the liquid and vapor phases, respectively. The momentum and energy equations,

$$\frac{\partial}{\partial t}(\rho \vec{u}) + \nabla \cdot (\rho \vec{u} \vec{u}) = -\nabla P + \nabla \cdot [\mu(\nabla \vec{u} + \nabla \vec{u}^T)] + \vec{F}_\sigma, \quad (2)$$

and

$$\frac{\partial}{\partial t}(\rho E) + \nabla \cdot (\vec{u}(\rho E + P)) = \nabla \cdot (k \nabla T) + Q, \quad (3)$$

respectively, are solved for the entire domain (including both the vapor and liquid) in which density, viscosity, and thermal conductivity in each cell are expressed as functions of the properties of individual phases weighted with respect to void fraction.

2.2.2. Surface Tension Model

Different surface tension models are available. In this study, the Continuum Surface Stress (CSS) model [69] is used. This model avoids any explicit calculation for curvature and could provide an anisotropic variant in modeling capillary forces based on surface stresses. It is also physically accurate in under-resolved regions such as sharp corners.

2.2.3. Turbulence Model

Different turbulence models have been adopted in previous two-phase CFD works as indicated in Tables 1 and 2. Among those, the Realizable $k-\epsilon$ turbulence model and the Shear-Stress Transport (SST) $k-\omega$ turbulence model [70] have been widely used in boiling simulations. In the present study, SST $k-\omega$ is used as it takes advantage of the standard $k-\omega$ turbulence model near the wall and the standard $k-\epsilon$ turbulence model away from the wall by means of a cross-diffusion term. Moreover, SST $k-\omega$ allows setting the value of interfacial turbulent damping. Damped cross-diffusion and a user defined turbulent viscosity are incorporated in the effective diffusivities term. Details of the SST $k-\omega$ model used in the study are provided elsewhere [55,71].

2.2.4. Phase Change Model

Lee [44] formulated separate conservation equations for the vapor and liquid phases and interactions based on the Hatlow-Amden two-fluid model [72]. As shown in Tables 1 and 2, the Lee model has been used extensively in recent flow boiling simulations. One drawback of this model is reliance on *mass transfer intensity factor*, γ , whose magnitude is not universal for different phase change situations and therefore must be adjusted based on system geometry, computational mesh, and operating conditions to tackle convergence issues and avoid unrealistically large temperature differences between interface and saturated vapor [73]. In the Lee model, the liquid-vapor mass transfer is expressed as

$$S_g = S_f = \gamma_g \alpha_g \rho_g \frac{(T - T_{sat})}{T_{sat}} \text{ for condensation } (T < T_{sat}) \quad (4a)$$

and

$$S_g = S_f = \gamma_f \alpha_f \rho_f \frac{(T - T_{sat})}{T_{sat}} \text{ for evaporation } (T > T_{sat}), \quad (4b)$$

where S_g , S_f , γ_g , and γ_f are the interfacial mass source term for evaporation, interfacial mass source term for condensation, mass transfer intensity factor for vapor, and mass intensity factor for liquid, respectively. For a cell containing liquid ($\alpha_f > 0$), and whose temperature is higher than saturation temperature, the liquid will be transferred to vapor. While, for a cell containing vapor ($\alpha_g > 0$), and whose temperature is lower than saturation temperature, the vapor will be condensed to liquid. Values of γ_g and γ_f in the present study are set at 100 s^{-1} for evaporation and 0.1 s^{-1} for condensation as recommended in recent work by Lee et al. [54].

2.2.5. Shear Lift Force

Among the many forces exerted on a bubble growing along a heated wall, Lee et al. [55] showed accurate prediction of interfacial behavior and heat transfer during flow boiling along a channel requires careful account for the shear-lift force. The shear-lift force formulation by Mei and Klausner [74] is adopted in the form of a source term in the momentum equation using a user-defined function (UDF) in ANSYS FLUENT. Details of the shear-lift coefficient [75,76] used and implementation of the source term are provided in [55].

2.3. Computational Domain

As discussed earlier, the horizontally-aligned heat sink considered in the study contains multiple parallel macro- or micro-channels, Fig. 1, and details of the geometrical parameters and operating conditions considered are provided in Table 3. To conduct a systematic comparison between micro- and macro-channel heat sinks, several parameters are held constant in each case, including base area, $25 \text{ mm} \times 25 \text{ mm}$ ($W \times L$), inlet liquid temperature, $T_{in} = 20^\circ\text{C}$, outlet pressure, $P_{out} = 120 \text{ kPa}$, base heat flux, and total flow rate. When comparing micro- to macro-channel heat sinks, corresponding values for number of channels, N , hydraulic diameter, D_h , and channel wall heat flux, q''_w , must satisfy the energy balance

$$q''_b LW = N_{micro} \pi D_{h,micro} L q''_{w,micro} = N_{macro} \pi D_{h,macro} L q''_{w,macro}. \quad (5)$$

With the heat sink width, W , fixed, the width of a cross-sectional cell containing one channel, w , (which is also the pitch between adjacent channels) is determined for the two heat sinks using

$$W = N_{micro} w_{micro} = N_{macro} w_{macro}. \quad (6)$$

Numerous combinations of D_h , N , and w satisfy Eqs. (5) and (6). The final matrix of cases considered in the study involve two hydraulic diameters, $D_h = 0.50 \text{ mm}$, representing a micro-channel heat sink for which $N = 20$ and $w = 1.25 \text{ mm}$, and $D_h = 5 \text{ mm}$,

representing a macro-channel heat sink with $N = 2$ and $w = 12.5 \text{ mm}$. Different combinations of q''_b , and Q_v are used to examine advantages and disadvantages of micro-channel versus macro-channel heat sinks over a range of operating conditions.

Fig. 2 shows the computational domain used, along with the boundary conditions and mesh structure. Simulations are performed for only a single channel of each heat sink to save computing time. This is based on assumption of axisymmetrically uniform heat flux, q''_w (obtained using Eq. (5)), along the channel wall. A key advantage of this assumption is avoiding performance differences between the two heat sinks resulting from thermal conductivity of the solid heat sink. Other than inability to capture conduction heat transfer details in the heat sink, focusing simulations on a single channel precludes assessment of possible parallel channel instabilities.

With all other parameters clearly defined, the channel wall heat flux, q''_w , is obtained using Eq. (5), and mass velocity, G , which is obtained from

$$\dot{m} = Q_v \rho_f = \frac{\pi}{4} N D_h^2 G. \quad (7)$$

Other parameters of interest that are included in Table 3 are thermodynamic equilibrium quality for at the channel inlet, $x_{e,in}$, and outlet, $x_{e,out}$, which are obtained, respectively, from

$$x_{e,in} = \frac{c_{p,f}(T_{in} - T_{sat})}{h_{fg}} \quad (8)$$

and

$$x_{e,out} = x_{e,in} + \frac{4q''_w L}{G h_{fg} D_h}, \quad (9)$$

based on fluid properties corresponding to a reference saturation pressure of $P_{sat} = 120 \text{ kPa}$. Notice that the $x_{e,in}$ values are not an exact representation of inlet fluid state since T_{sat} should be based on inlet pressure, P_{in} , which is not known in advance. Similarly, the $x_{e,out}$ values are not exact because of their dependence on $x_{e,in}$. Therefore the $x_{e,in}$ and $x_{e,out}$ values in Table 3 are intended only to provide some indication of fluid states at the inlet and outlet.

2.4. Grid Independence

An axisymmetric CFD domain spanning the entire diameter of the channel is used instead of relying on symmetry with a half domain extending from the axis to the wall (see Fig. 2). This provides independency in bubble production and interfacial behavior on either side of the axis [67,68,77].

Since mesh quality is known to have a profound influence on the accuracy of fluid flow and heat transfer simulations, it is of paramount importance to choose a grid size that does not influence computed results. Different meshes are attempted in GAMBIT software [78] (and further refined in ANSYS FLUENT [68]) which consist of a uniform structure in the core region and gradually become non-uniform and finer near the wall. Fig. 3(a) shows axial variation of wall temperature for $D_h = 0.5 \text{ mm}$ (micro-channel), $G = 500 \text{ kg/m}^2\text{s}$, and $q''_w = 24 \text{ W/cm}^2$ predicted using the consolidated theoretical/empirical method (to be discussed in a later section) and the computational model, the latter using three different grid sizes. Fig. 3(b) shows, for the same operating conditions and both the theoretical/empirical and computational models, variations of average wall temperature with grid size. Overall, good convergence as well as agreement with the theoretical/empirical results is achieved below a grid size of $\Delta c = 0.02 \text{ mm}$ (for the core region). Therefore, mesh 1, with $\Delta c = 0.01 \text{ mm}$ for the core region is used throughout the study. This mesh corresponds to 267,500 quadrilateral cells and 275,106 nodes. It is important to note this mesh size shows similar convergence for the macro-channel.

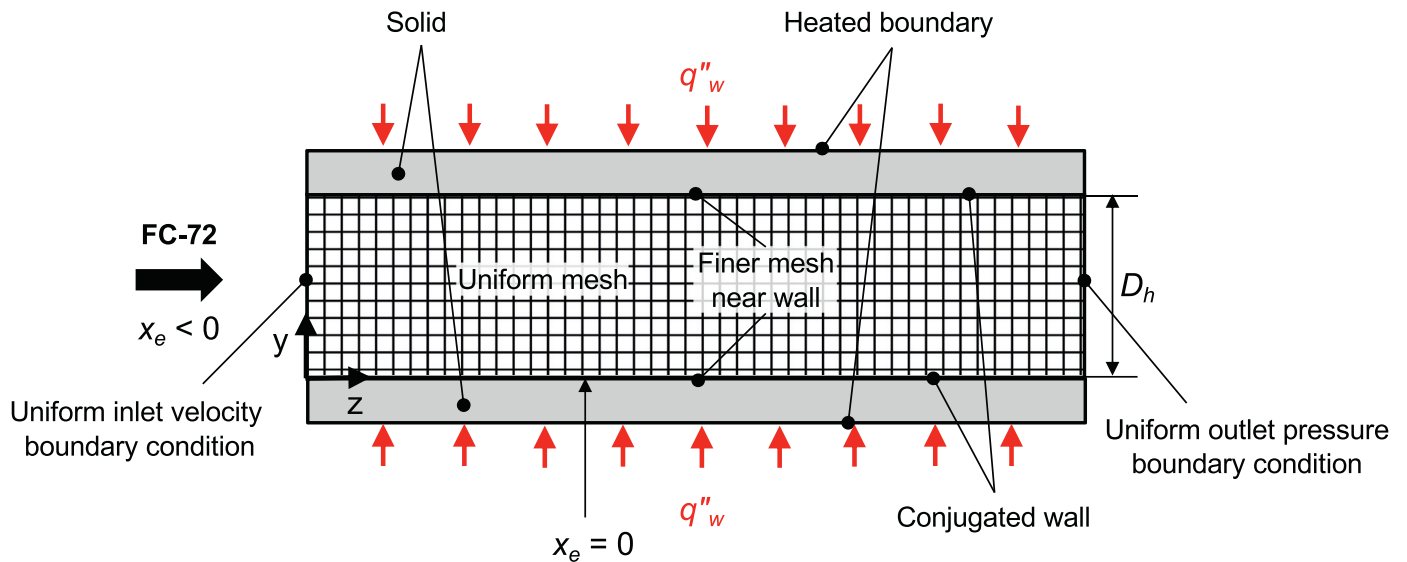


Fig. 2. Computational domain, boundary conditions, and mesh structure used in the simulations.

Since velocity and temperature gradients are steepest near the wall, it is important that the first mesh layer be small enough to accurately capture these gradients. This is achieved by maintaining non-dimensional distance y^+ ($=yu_\tau/\nu_f$) from the wall below 5. Fig. 4 shows, using mesh 1, this criterion is satisfied for both the micro- and macro-channels, with average y^+ values of 0.989 and 0.675, respectively, and maximum values for both below 5 along the entire channel.

2.5. Complete Model Formulation for Simulations

All simulations are conducted using FC-72, a 3M Company dielectric coolant popular for direct immersion cooling of electronic and power devices. Thermophysical properties of this fluid are obtained from NIST Standard Reference Database 23 [79], and fitted as polynomial functions of temperature and/or pressure in FLUENT. The coolant is assumed to enter the channel in subcooled liquid state at $T_{in} = 20^\circ\text{C}$ and a uniform inlet velocity is adopted with turbulent intensity calculated according to $I = u'/\bar{u} = 0.16\text{Re}_D^{-1/8}$, and exit with a uniform outlet pressure of $P_{out} = 120$ kPa. A non-slip condition is applied to the channel wall, with a constant wall heat flux assumed for the entire channel length. Recognizing that conjugate heat transfer along the wall is important to preventing near-wall numerical errors [55], the computational domain is extended to include a 0.50-mm layer of solid wall material (a thermal conductivity value equal to that of pure copper is used).

The pressure-based coupled solver with absolute velocity formulation is selected in FLUENT. The transient VOF multiphase model with explicit scheme is adopted with the default volume fraction cutoff of 10^{-6} and Courant number of 0.25. Implicit body formulation is enabled to improve solution convergence and double precision is used to improve accuracy of the VOF model. Geometric Reconstruction Scheme is selected to obtain the face fluxes. Scalar values at cell faces are constructed, and velocity derivatives and secondary diffusion terms are computed by Least Squares Cell-Based Gradient Evaluation. Pressure Staggering Option PRESTO is chosen for spatial discretization in the VOF model, and Implicit Time Integration is adopted for spatial and temporal discretization in governing equations. First-Order Upwind Scheme is selected for specific dissipation rate and turbulent kinetic energy discretization, and Second-Order Upwind Scheme for momentum and energy discretization. The under-relaxation factors and explicit relaxation factors are carefully adjusted to improve convergence. The conver-

gence criteria are 10^{-5} for the continuity equation, and 10^{-6} for the momentum, energy, and turbulence equations.

3. Consolidated Theoretical/Empirical Methods

3.1. Overview of the Methods

The consolidated theoretical/empirical methods used to predict steady-state pressure drop and heat transfer are based largely on one proposed by Kim and Mudawar [80] for flow boiling in channels. These methods possess the capability of tackling transport behavior across all possible flow regimes from inlet to outlet. In most two-phase thermal management applications, the coolant is introduced in subcooled liquid state and, as it flows through the channel, heat transfer transitions from single-phase liquid convection to subcooled boiling to saturated boiling (also theoretically to single-phase vapor convection, though this is not desirable in thermal management applications).

A typical heat sink contains an array of parallel channels sharing inlet and outlet plenums. While this configuration may promote flow instabilities (e.g., parallel channel instability), causing temporal differences in flow pattern between channels [81,82], the present consolidated methods are built on the assumption that flow behavior is identical in all the channels, and are therefore not intended to address instabilities. The total mass flow rate to the entire heat sink is assumed to split evenly among all channels and the base heat flux conducted uniformly to all channel walls. A single channel is divided into small discrete axial segments of equal lengths. Steady state calculations are performed in a one-dimensional fashion and cross-sectional variations within the segments are ignored. Thermophysical properties are estimated based on local fluid temperature. Finally, gravitational effects are ignored.

3.2. Pressure Drop

A comprehensive list of equations used to predict pressure drop for two-phase heat sinks is presented in Table 4. Total pressure drop across the heat sink, ΔP_{tot} , is the sum of several components: inlet contraction (pressure loss), ΔP_c , upstream single-phase liquid region, $\Delta P_{sp,f}$, two-phase subcooled boiling region, ΔP_{sc} , two-phase saturated boiling region, ΔP_{sb} , downstream single-phase vapor region, $\Delta P_{sp,g}$, and outlet expansion (pressure recovery), ΔP_e . It should be noted that not all these components are present in

Table 4
Theoretical/empirical relations used to predict pressure drop in two-phase heat sinks.

Total Pressure Drop	
$\Delta P_{tot} = \Delta P_{sp,f} + \Delta P_{tp} + \Delta P_{sp,g}$; $\Delta P_{tp} = \Delta P_{sc} + \Delta P_{sb}$	
Single-phase liquid pressure drop	
$\Delta P_{sp,f} = \frac{2f_{app}G^2L_{sp,f}v_f}{D_h}; Re_{sp,f} = \frac{GD_h}{\mu_f}$	
Laminar hydrodynamically developing regime [85]	
$f_{app}Re_{sp} = \left\{ \left[3.2 \left(\frac{L_{sp}}{Re_{sp}D_h} \right)^{-0.57} \right]^2 + (f_{sp}Re_{sp})^2 \right\}^{1/2}$	
Laminar fully developed regime $f_{sp,f}Re_{sp,f} = 16$	
Turbulent hydrodynamically developing regime [86]	
$\frac{L_{sp}}{D_h} = 1.4039Re_{sp}^{0.25}\delta^{+1.25} \left(1 + 0.1577\delta^{+} - 0.1793\delta^{+2} \dots \right)$ $\left(-0.0168\delta^{+3} + 0.0064\delta^{+4} \right)$	
$f_{app} = \left[\frac{1}{(1 - 0.25\delta^{+} + 0.0667\delta^{+2})^2} - 1 \right] \frac{0.25}{L_{sp}/D_h}$ in turbulent developing regime ($\delta^{+} < 1$)	
$f_{app} = \left(0.07 + 0.316 \frac{L_{sp}/D_h}{Re_{sp}^{0.25}} \right) \frac{0.25}{L_{sp}/D_h}$ in turbulent developed regime ($\delta^{+} = 1$)	
Turbulent fully developed regime [87] $f_{sp,f} = \begin{cases} 0.079 Re_{sp,f}^{-0.25}, & 2000 \leq Re_{sp,f} < 20000 \\ 0.046 Re_{sp,f}^{-0.2}, & Re_{sp,f} \geq 20000 \end{cases}$	
Two-phase subcooled boiling pressure drop [80]	
$\frac{\Delta P_{sc}}{\Delta P_{ad}} = 20.73 Ja^{*-0.98} \beta^{0.42} \left(\frac{L}{D_h} \right)^{-0.54} \frac{L_{sc}}{L_{sc,max}}; Ja^{*} = \frac{c_{p,f} \Delta T_{sub,in}}{h_{fg}}; \beta = 1;$	
$L_{sc,max} = \frac{GA_c}{q''_w P_H} c_{p,f} (T_{sat} - T_f)_{in}$	
Two-phase saturated boiling pressure drop	
<i>Method 1: Homogeneous Equilibrium Model (HEM)</i>	
$-\left(\frac{dP}{dz} \right) = \frac{\tau_F P_F + G^2 v_{fg} \frac{dx_e}{dz} + \frac{g \sin \theta}{x_e v_g + (1 - x_e) v_f}}{1 + G^2 [x_e \frac{dv_g}{dP} + (1 - x_e) \frac{dv_f}{dP}]}$	
$-\left(\frac{dP}{dz} \right) = \frac{\left\{ 1 + \frac{G^2 v_{fg}}{h_{fg}} [x_e v_g + (1 - x_e) v_f] \right\} \frac{\tau_F P_F + G v_{fg} \left(\frac{q''_w P_H}{A_c h_{fg}} \right) + \frac{g \sin \theta}{x_e v_g + (1 - x_e) v_f}}{1 + \frac{G^2 v_{fg}}{h_{fg}} [x_e v_g + (1 - x_e) v_f]} + G^2 \left[x_e \frac{dv_g}{dP} + (1 - x_e) \frac{dv_f}{dP} \right] - \frac{G^2 v_{fg}}{h_{fg}} \left[x_e \frac{dh_g}{dP} + (1 - x_e) \frac{dh_f}{dP} \right]}$	
$\tau_F = \frac{1}{2} f_{tp} (v_f + x_e v_{fg}) G^2; f_{tp} = \begin{cases} 16/Re_{tp}, & Re_{tp} < 2000 \\ 0.079 Re_{tp}^{-0.25}, & 2000 \leq Re_{tp} < 20000; Re_{tp} = \frac{GD_h}{\mu_{tp}} \\ 0.046 Re_{tp}^{-0.2}, & Re_{tp} \geq 20000 \end{cases}$	
$\mu_{tp} = \omega \mu_g + (1 - \omega)(1 + 2.5\omega)\mu_f; \omega = \frac{x_e v_g}{v_f + x_e v_{fg}} \quad [90]$	
<i>Method 2: Separated Flow Model (SFM)</i>	
$\Delta P_{sb} = \Delta P_{sb,A} + \Delta P_{sb,F}; \Delta P_{sb,A} = G^2 \left\{ \left[\frac{v_g x_{e,out}^2}{\alpha_{out}} + \frac{v_f (1 - x_{e,out})^2}{(1 - \alpha_{out})} \right] - \left[\frac{v_g x_{e,in}^2}{\alpha_{in}} + \frac{v_f (1 - x_{e,in})^2}{(1 - \alpha_{in})} \right] \right\};$	
$\alpha = \left[1 + \left(\frac{1 - x_e}{x_e} \right) \left(\frac{v_f}{v_g} \right)^{2/3} \right]^{-1} \quad [91]; -\left(\frac{dP}{dz} \right)_F = \begin{cases} -\left(\frac{dP}{dz} \right)_{F,f} \phi_f^2, & -\left(\frac{dP}{dz} \right)_{F,f} \phi_f^2 > -\left(\frac{dP}{dz} \right)_{F,g} \phi_g^2 \\ -\left(\frac{dP}{dz} \right)_{F,g} \phi_g^2, & -\left(\frac{dP}{dz} \right)_{F,g} \phi_g^2 > -\left(\frac{dP}{dz} \right)_{F,f} \phi_f^2 \end{cases};$	
$\phi_f^2 = 1 + \frac{C}{X} + \frac{1}{X^2}; \phi_g^2 = 1 + CX + X^2; -\left(\frac{dP}{dz} \right)_{F,f} = \frac{2 f_f G^2 (1 - x_e)^2 v_f}{D_h};$	
$-\left(\frac{dP}{dz} \right)_{F,g} = \frac{2 f_g G^2 x_e^2 v_g}{D_h}; X = \left[-\left(\frac{dP}{dz} \right)_{F,f} / -\left(\frac{dP}{dz} \right)_{F,g} \right]^{0.5}$	
$f_k = \begin{cases} 16/Re_k, & Re_k < 2000 \\ 0.079 Re_k^{-0.25}, & 2000 \leq Re_k < 20000; Re_f = \frac{(1 - x_e) G D_h}{\mu_f}; Re_g = \frac{x_e G D_h}{\mu_g} \\ 0.046 Re_k^{-0.2}, & Re_k \geq 20000 \end{cases}$	
$C = \begin{cases} C_{non-boiling} \left[1 + 60 We_{fo}^{0.32} \left(Bo \frac{P_H}{P_F} \right)^{0.78} \right], & Re_f \geq 2000 \\ C_{non-boiling} \left[1 + 530 We_{fo}^{0.52} \left(Bo \frac{P_H}{P_F} \right)^{1.09} \right], & Re_f < 2000 \end{cases} \quad [89]$	
$C_{non-boiling} = \begin{cases} 0.39 Re_{fo}^{0.03} Su_{go}^{0.10} (\rho_f / \rho_g)^{0.35}, & Re_f \geq 2000, Re_g \geq 2000 (tt) \\ 8.7 \times 10^{-4} Re_{fo}^{0.17} Su_{go}^{0.50} (\rho_f / \rho_g)^{0.14}, & Re_f \geq 2000, Re_g < 2000 (tv) \\ 0.0015 Re_{fo}^{0.59} Su_{go}^{0.19} (\rho_f / \rho_g)^{0.36}, & Re_f < 2000, Re_g \geq 2000 (vt) \\ 3.5 \times 10^{-5} Re_{fo}^{0.44} Su_{go}^{0.50} (\rho_f / \rho_g)^{0.48}, & Re_f < 2000, Re_g < 2000 (vv) \end{cases}$	
$Re_{fo} = \frac{GD_h}{\mu_f}; Su_{go} = \frac{\rho_g \sigma D_h}{\mu_g^2}; We_{fo} = \frac{G^2 D_h}{\rho_f \sigma}; Bo = \frac{q''_w}{G h_{fg}}$	

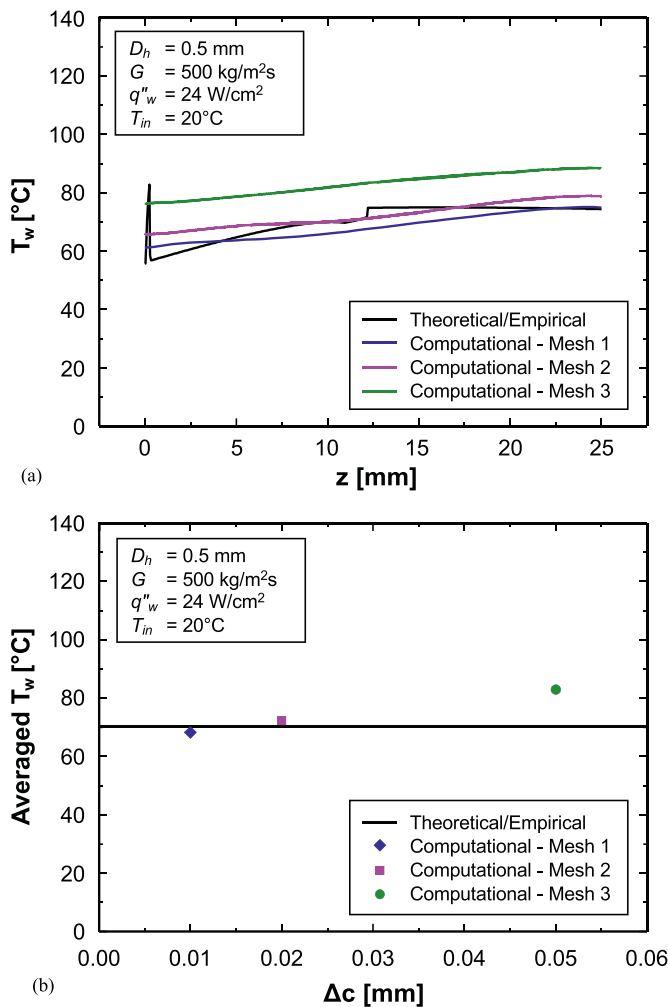


Fig. 3. Grid independence test based on (a) axial variation of wall temperature and (b) average wall temperature.

every case. The contributions of individual components are determined by the heat sink's geometry and operating conditions. For example, the heat sink may be not long enough for flow to become saturated or superheated and may even exit the heat sink in subcooled state. In this study, effects of inlet and outlet plenums are not considered for simplicity, and to maintain identity with the CFD simulations.

3.2.1. Single-phase Liquid Pressure Drop

Since the fluid enters the channel in subcooled liquid state, the length of the single-phase liquid region, L_{sp} , extends from the inlet to the axial location of Onset of Nucleate Boiling (ONB), which is determined according to a relation by Sato and Matsumura [83],

$$q''_{w,ONB} = \frac{k_f h_{fg} \rho_g (T_{w,ONB} - T_{sat})^2}{8 \sigma T_{sat}} \quad (10)$$

Pressure drop in the upstream single-phase liquid region is calculated using the apparent single-phase friction factor, f_{app} , whose value is based on liquid Reynolds number, $Re_{sp,f}$. For the laminar hydrodynamically developing region, f_{app} is determined using an empirical formula of the Churchill and Usagi [84] type obtained by Copeland [85]. For the turbulent hydrodynamically developing regime, Zhi-qing's [86] analytical solution for a circular tube is used. The non-dimensional turbulent boundary layer thickness, δ^+ , is determined, using which, the apparent friction factor is calculated for the turbulent developing region ($\delta^+ < 1$) and turbulent developed region ($\delta^+ = 1$) using the respective relations.

In special cases where the flow entering the channel is laminar ($Re_{sp,f,in} < 2000$) and turns turbulent ($Re_{sp,f} \geq 2000$) downstream, the friction factor in the turbulent region is computed using the Blasius and McAdams relations [87] for fully developed flow corresponding to $2000 \leq Re_{sp,f} < 20000$ and $Re_{sp,f} \geq 20000$. This type of transition to turbulent flow usually results from a drastic change in liquid viscosity along the channel.

3.2.2. Subcooled Boiling Pressure Drop

The ratio of subcooled boiling pressure drop to that for adiabatic single-phase flow is determined with an empirical correlation by Kim and Mudawar [80] using a channel aspect ratio of

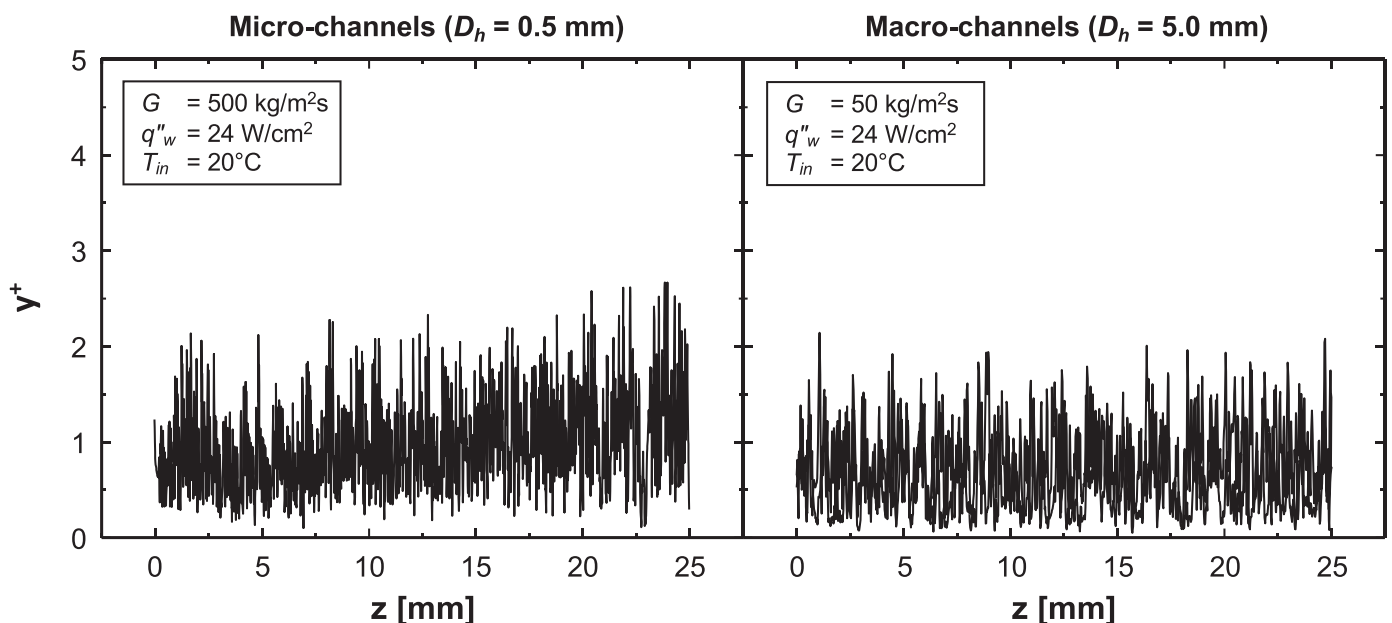


Fig. 4. Streamwise variations of y^+ using $\Delta c = 0.02$ mm for micro- and macro-channels with an identical flow rate of $Q_v = 76.59$ mL/min and base heat flux of $q''_b = 30.16$ W/cm².

unity. The subcooled boiling length, L_{sc} , is defined as that extending from the ONB location to the channel exit for cases where the fluid never reaches saturation, or to the point where the fluid reached $x_e = 0$, where the fluid exits the channel in saturated state. $L_{sc,max}$ is the length from the ONB location to a hypothetical location where $x_e = 0$; $L_{sc,max} = L_{sc}$ for all conditions of the present study since the fluid exits the heat sink in saturated state.

3.2.3. Two-phase Saturated Boiling Pressure Drop

Pressure drop in the saturated boiling regime is determined using two widely popular models: the Homogeneous Equilibrium Model (HEM) and the Separated Flow Model (SFM).

Homogeneous Equilibrium Model - The Homogeneous Flow Model treats a two-phase mixture as a pseudo single-phase fluid that obeys simple conservation equations, but with properties that are averaged between those of the liquid and vapor. The Homogeneous Equilibrium Model (HEM) is a special case of the Homogeneous Flow Model, where thermodynamic equilibrium quality, x_e , is assumed to equal the flow quality, x , for saturation conditions, and only latent heat can be exchanged between the two phases [88]. A relation for pressure gradient, $-(dP/dz)$, is derived by applying mass, momentum, and energy conservation to a differential control volume of axial length Δz . The wall shear stress, τ_f , in the momentum equation is determined using a two-phase friction factor, f_{tp} . Various methods for evaluating f_{tp} have been proposed, the simplest being assignment of a constant value. Another method is to use a relation for two-phase mixture viscosity, μ_{tp} , in two-phase Reynolds number, Re_{tp} . Different techniques have been proposed to evaluate μ_{tp} , some of which satisfy the limiting conditions of $\mu_{tp} = \mu_f$ at $x_e = 0$ and $\mu_{tp} = \mu_g$ at $x_e = 1$ while others do not. Kim and Mudawar [27,89] assessed the predictive performance of numerous mixture viscosity relations against their large consolidated pressure drop databases for adiabatic two-phase flow, as well as boiling and condensing flows; these databases encompass a large number of fluids and broad ranges of geometrical parameters and operating conditions. Different mixture viscosity relations provided best predictions in each of the four regimes of laminar liquid-laminar vapor (lv), laminar liquid-turbulent vapor (lt), turbulent liquid-laminar vapor (tl), and turbulent liquid-turbulent vapor (tt). But a mixture viscosity relation by Beattie and Whalley [90] provided best overall predictions. This relation is therefore adopted in the present study when using HEM to predict pressure drop for the saturated boiling region.

Separated Flow Model - The Separated Flow Model (SFM) treats the two-phase flow as consisting of two discrete phases, each with its individual properties and velocities [88]. Neglecting gravity effects, pressure drop for two-phase saturated boiling, ΔP_{sb} , is comprised of accelerational and frictional components. The accelerational component, $\Delta P_{sb,A}$, is evaluated using Zivi's void fraction correlation [91]. As to the frictional component, $\Delta P_{sb,F}$, most recent SFM 'semi-empirical' correlations are based on the Lockhart-Martinelli method [92]. To determine $\Delta P_{sb,F}$, the frictional pressure gradient of the two-phase mixture is expressed as the product of the frictional pressure gradient for one phase and a two-phase multiplier, ϕ_k [89], which, in turn, is a function of the Lockhart-Martinelli parameter, X . In the present study, determining $\Delta P_{sb,F}$ using SFM is based on the universal correlations of Kim and Mudawar [89].

3.2.4. Single-phase Vapor Pressure Drop

A single-phase vapor region is encountered in the downstream portion of the channel if $x_e = 1$ occurs before the outlet. This region is rarely seen in practical heat sinks as CHF occurs upstream of $x_e = 1$, and heat flux is set safely below CHF to avoid physical burnout of the device being cooled.

Table 5

Theoretical/empirical relations used to predict heat transfer in two-phase heat sinks.

Single-phase liquid region	
Laminar regime	$Nu_z = \left\{ \left[1.54 \left(\frac{L_{sp,f}}{Re_{sp,f} Pr_f D_h} \right)^{-0.33} \right]^4 + Nu_{lam,f}^4 \right\}^{1/4} \quad [85]; Nu_{lam,f} = 4.364$
Turbulent regime	$Nu_z = Nu_{turb,f} \left[1 + \frac{(L_{sp}/D_h)^{-0.9}}{10 Pr_f^{1/6}} \left(0.68 + \frac{3000}{Re_{sp,f}^{0.81}} \right) \right] \quad [93];$ $Nu_{turb,f} = 0.023 Re_{sp,f}^{0.8} Pr_f^{0.4} \quad [94,95]; Re_{sp,f} = \frac{GD_h}{\mu_f}$
Two-phase subcooled boiling region [97]	
	$\frac{Nu_{sc}}{Nu_{sp}} = 78.5 \left(\frac{q''_w}{h_{fg} \rho_g u_f} \right)^{0.67} \left(\frac{h_{fg}}{c_{p,f} \Delta T_{sub}} \right)^{0.5} \left(\frac{\rho_g}{\rho_f} \right)^{0.7} \left(\frac{c_{p,f} \mu_f}{k_f} \right)^{0.46}$
Two-phase saturated boiling region [29]	
	$h_{sb} = (h_{nb}^2 + h_{cb}^2)^{0.5};$ $h_{nb} = \left[2345 \left(Bo \frac{P_H}{P_f} \right)^{0.70} P_R^{0.38} (1 - x_e)^{-0.51} \right] \left(0.023 Re_f^{0.8} Pr_f^{0.4} \frac{k_f}{D_h} \right);$ $h_{cb} = \left[5.2 \left(Bo \frac{P_H}{P_f} \right)^{0.08} We_{fo}^{-0.54} + 3.5 \left(\frac{1}{X_{tt}} \right)^{0.94} \left(\frac{\rho_g}{\rho_f} \right)^{0.25} \right] \left(0.023 Re_f^{0.8} Pr_f^{0.4} \frac{k_f}{D_h} \right);$ $Bo = \frac{q''_w}{G h_{fg}}; P_R = \frac{P}{P_{crit}}; Re_f = \frac{G(1 - x_e) D_h}{\mu_f}; We_{fo} = \frac{G^2 D_h}{\rho_f \sigma};$ $X_{tt} = \left(\frac{\mu_f}{\mu_g} \right)^{0.1} \left(\frac{1 - x_e}{x_e} \right)^{0.9} \left(\frac{\rho_g}{\rho_f} \right)^{0.5}$

3.3. Heat Transfer Coefficient

Similar to pressure drop, heat transfer calculations are performed for the different regions of the channel length. Table 5 provides a comprehensive list of equations used to predict heat transfer for all the regions. They are presented in terms of either heat transfer coefficient or Nusselt number.

3.3.1. Single-phase Liquid Region

The upstream single-phase liquid region is assumed to be thermally developing as it is relatively short in practical two-phase heat sinks. Local Nusselt numbers for the thermally developing laminar and turbulent regions are calculated, respectively, in accordance with relations by Copeland [85] and Al-Arabi [93] for constant wall heat flux. And, Nusselt number for the fully developed turbulent region is determined according to the relation of Dittus and Boelter [94,95].

3.3.2. Two-phase Subcooled Boiling Region

Heat transfer for the subcooled boiling region is typically expressed as ratio of two-phase Nusselt number to single-phase Nusselt number. Prior assessments of subcooled boiling Nusselt number correlations for micro-channels [81] and conventional-sized annuli [96] showed best predictions of experimental data are achieved using an empirical correlation by Moles and Shaw [97]. This correlation is therefore used in the present study. It is important to note, however, that, in this correlation, the Nusselt number is proportional to a negative power of the degree of subcooling. This produces a singularity at the point of saturation and very high artificial values for the heat transfer coefficient near saturation conditions. Corrections have been made to address this issue with a linear extrapolation of h_{sc} between $x_e = -0.05$ and 0 based on h values at $x_e = -0.1$ and -0.05 , details for which are provided in [98].

3.3.3. Two-phase Saturated Boiling Region

The heat transfer coefficient for the saturated boiling region, h_{sb} , is determined using the universal correlation by Kim and Mu-

Table 6
Summary of consolidated theoretical/empirical prediction methods used for comparison with CFD simulations.

Plot color	Subcooled boiling pressure drop	Saturated boiling pressure drop	Subcooled boiling heat transfer	Saturated boiling heat transfer
Green	Kim & Mudawar subcooled boiling correlation [80]	HEM; Beattie & Whalley's mixture viscosity model [90]		
Red	Kim & Mudawar subcooled boiling correlation [80]	SFM; Kim & Mudawar's universal correlation [89]	Moles & Shaw's empirical correlation [97]	Kim & Mudawar's universal correlation [29]
Blue	Single-phase liquid assumption	HEM; Beattie & Whalley mixture viscosity model [90]		
Pink	Single-phase liquid assumption	SFM; Kim & Mudawar's universal correlation [89]		

dawar [29], in which it is expressed as the square root mean of heat transfer coefficients for nucleate boiling and convective boiling dominant regions of saturated boiling. Use of this correlation is justified by its reliance on data for a large variety of fluids and broad ranges of geometrical parameters and operating conditions.

3.3.4. Single-phase Vapor Region

Local Nusselt numbers in the downstream single-phase vapor region for laminar and turbulent flows are given by respective fully developed flow relations. As indicated earlier, this region is rarely seen in practical heat sinks.

3.4. Theoretical/Empirical Predictions for Comparison with CFD Results

The theoretical/empirical prediction techniques for pressure drop and heat transfer discussed thus far are executed over each small channel segment from inlet to outlet. All boundary conditions are identical to those used in the CFD simulations except for inlet pressure, P_{in} , which is set equal to that obtained from the simulation results. Since, as shown in Table 3, the simulations are based on an inlet temperature of $T_{in} = 20^\circ\text{C}$ and outlet pressure of $P_{out} = 120$ kPa, the computed inlet pressure is slightly different for each case. The theoretical/empirical calculations are executed using four different combinations of sub-models which are summarized in Table 6, two based on HEM and two SFM. Another difference between the different combinations is in treatment of pressure drop in the subcooled boiling region.

4. Results and Discussion

4.1. Time-Dependent Computational Results

An essential aspect of the CFD simulations is to investigate time-dependent predictions of the variations of fluid temperature and interfacial behavior and make certain that steady state conditions are indeed achieved. Fig. 5 shows predicted transverse profile of fluid outlet temperature, T_{out} , for the micro- and macro-channels for identical operating conditions and gradually increasing computing time. As time advances, the heating effect is felt deeper into the core region causing an increase in average T_{out} . Convergence to a steady state is achieved after a certain time, beyond which fluid temperature shows only variations about the same mean. The primary reason for the profile distortions about the mean is passage of vapor bubbles entrained in the bulk flow. The larger distortions for the macro-channels are the outcome of a larger number of smaller bubbles, as will be shown later. Notice the longer computing time required for the macro-channels to reach steady state. This is the result of a larger amount of subcooled liquid in the core region of macro-channels needing more time to condense the generated bubbles. It should be noted that convergence time is determined on a case by case basis using both the temperature profiles just mentioned and flow pattern plots, as discussed below.

Fig. 6 shows an example of the evolution of flow patterns with computing time for the micro-channels at $G = 500$ kg/m²s and $q''_w = 24$ W/cm². Bulk fluid enters the channel in subcooled liquid state and begins to gain sensible heat from the wall. Liquid adjacent to the wall heats up faster than the still subcooled core. Eventually, the wall liquid is heated above local saturation temperature, causing upstream bubble formation corresponding the Onset of Nucleate Boiling (ONB). In early times, the core subcooling confines the bubble nucleation process to very small bubbles along the wall. As time advances, the location of ONB moves upstream at the expense of a shorter upstream single-phase liquid region because of more fluid sensing the heating from the wall. Some of the bubbles are seen sliding along the wall because of axial momentum of the liquid, but still maintaining contact with the wall because of surface tension effects. With time, and also at the same time but farther downstream, the bubbles, having acquired larger size, begin to detach from the wall and move towards the core region where shear stresses are weaker. Some of the bubbles condense after departure because of the condensation effects offered by the subcooled bulk flow. Other bubbles condense back to liquid before they can depart from the wall. These trends are a reflection of the fact that evaporation and condensation occur simultaneously in subcooled flow boiling [81]. As more heat is added to the bulk fluid along the channel, the degree of local subcooling decreases and the fluid tends toward a saturated state, at which the bulk condensation effects diminish greatly, enabling more bubbles to grow within the core. Formation of large bubbles is shown to result from coalescence of smaller ones. Notice how, at $t = 0.5473$ s, the larger bubbles now occupy the entire flow area. This constitutes the beginning of slug flow, which is characterized by liquid slugs trapped between consecutive 'bullet-shaped' vapor bubbles, each having a hemispherical front and a rather flat tail. A thin layer of liquid exists circumferentially around the oblong bubbles. Both the liquid layer and the liquid slugs continue to evaporate, leading to yet longer vapor bubbles, as seen at $t = 0.6283$ s, where interfacial behavior has reached steady state. It is important to note that different operating conditions produce different flow patterns, and sufficient computing time is allowed for each set of operating conditions and each of the micro- and macro-channels to ensure attainment of steady state.

4.2. Flow Pattern Results

Fig. 7 shows computed flow patterns along both the micro- and macro-channels for all operating conditions in Table 3. In all cases, subcooled liquid enters the channel with an inlet temperature of $T_{in} = 20^\circ\text{C}$ and a corresponding thermodynamic equilibrium quality of $x_{e,in} = -0.498$ ($x_{e,in}$ is approximate since P_{in} varies slightly based on pressure drop for each case). Vapor production and evolution are fairly symmetrical about the central axis (evident mostly for the micro-channels), a result of ignoring gravity effects. Minor asymmetries are the result of small-scale turbulence effects as well as passage of vapor bubbles. Both micro- and macro-channels

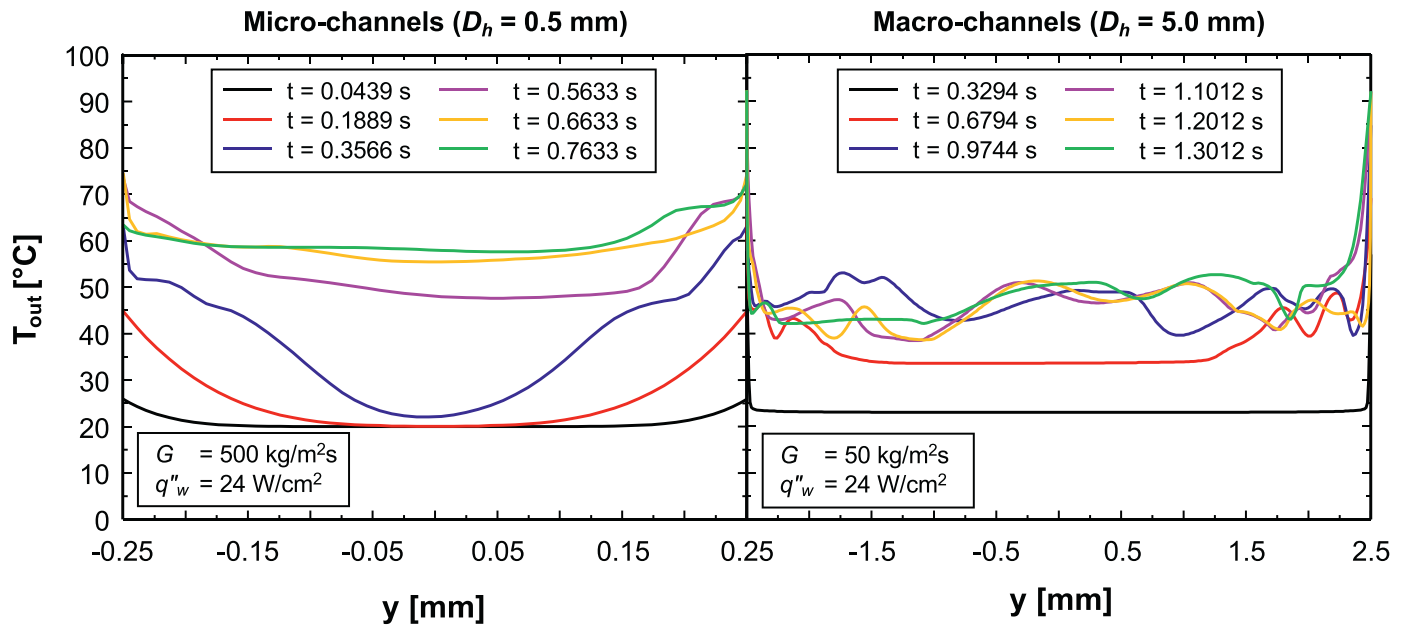


Fig. 5. Evolution of outlet fluid temperature profile for micro- and macro-channels with increasing computing time for $T_{in} = 20^{\circ}\text{C}$, $q''_b = 30.16 \text{ W/cm}^2$, and a flow rate of $Q_v = 76.59 \text{ mL/min}$.

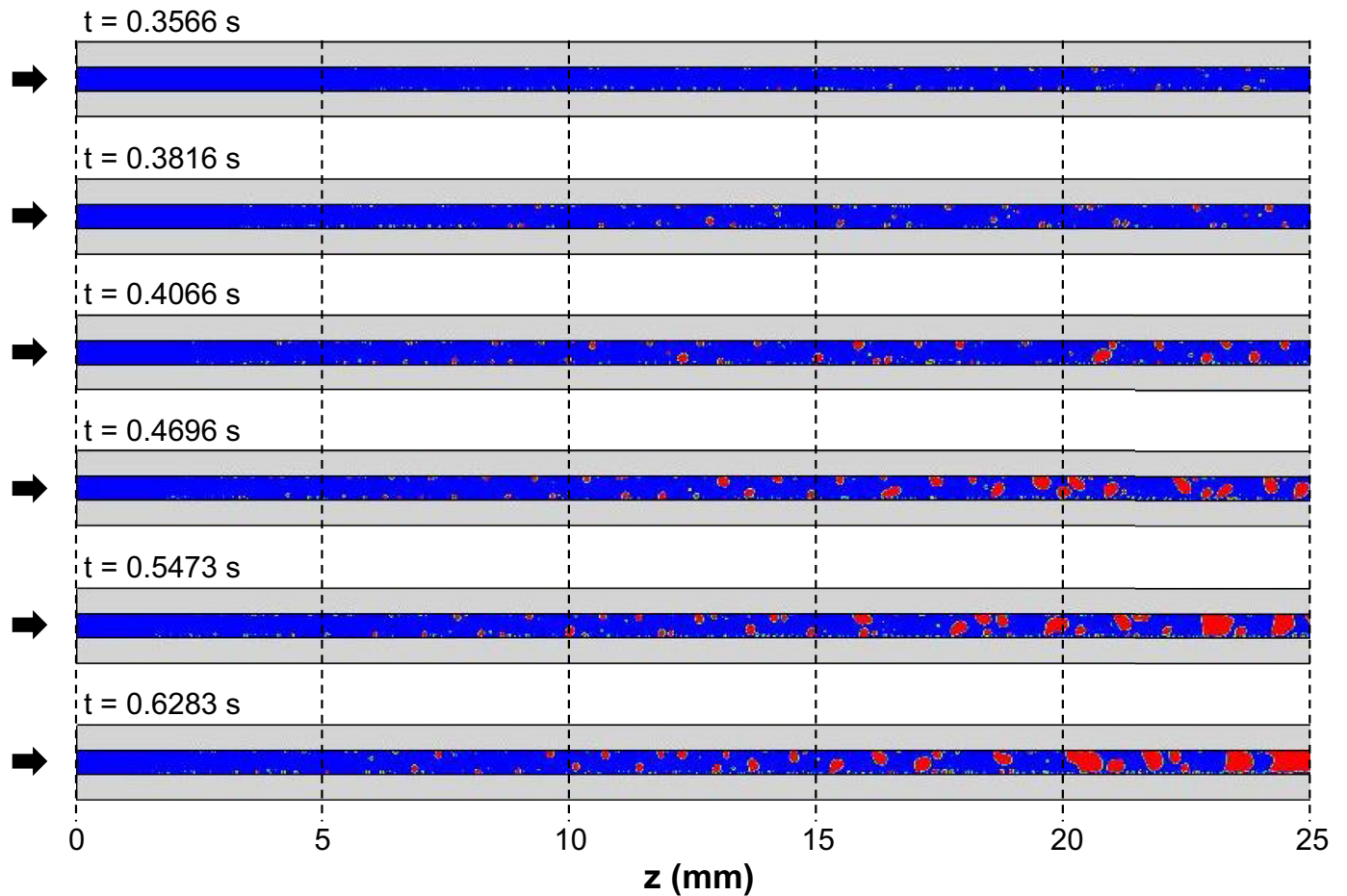


Fig. 6. Evolution of micro-channel flow patterns with increasing computing time for $G = 500 \text{ kg/m}^2\text{s}$ and $q''_w = 24 \text{ W/cm}^2$.

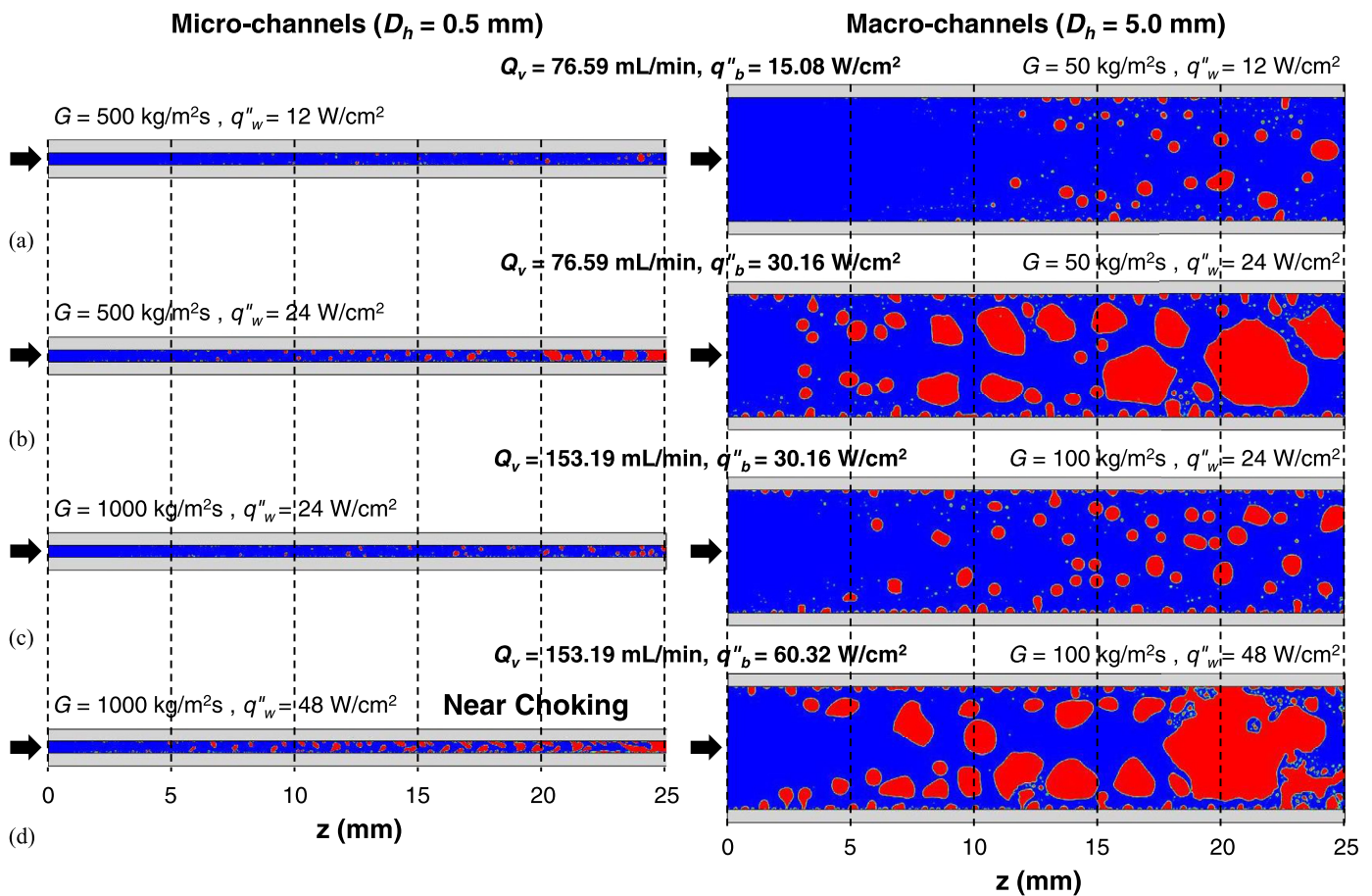


Fig. 7. Computationally predicted flow patterns in micro- and macro-channels for (a) $Q_v = 76.59$ mL/min with $q''_b = 15.08$ W/cm², (b) $Q_v = 76.59$ mL/min with $q''_b = 30.16$ W/cm², (c) $Q_v = 153.19$ mL/min with $q''_b = 30.16$ W/cm², and (d) $Q_v = 153.19$ mL/min with $q''_b = 60.32$ W/cm².

show a long upstream single-phase liquid region for the lower flow rate and lower heat flux. For a fixed flow rate, the single-phase length grows shorter at the higher heat flux because of earlier formation of bubbles resulting from higher temperature liquid close to the wall. For all operating conditions, serried bubbles can be seen downstream leading to coalescence and flow regime transitions. Higher vapor content at the higher heat flux allows formation of multiple flow regimes. For the micro-channels and both mass velocities, exit conditions for the lower and higher heat flux cases are seen dominated by bubbly flow and slug flow, respectively. And, for both channels, the shape of bubbles is more uniform at lower mass velocities because of weaker inertial and shear forces. For all cases, the shape of the vapor bubbles becomes increasingly more distorted downstream because of axial acceleration of the flow, in addition to more pronounced turbulence effects.

4.3. Fluid Velocity Results

Figs. 8(a) and 8(b) show, for flow rates of $Q_v = 76.59$ and 153.19 mL/min, respectively, a comparison of computationally predicted, temporally and cross-sectionally averaged fluid velocity profiles for micro- and macro-channels. Average velocity in two-phase flow is a function of both mass velocity and local void fraction. Figs. 8(a) and 8(b) show that, for a fixed total flow rate, the velocity is higher in micro-channels because of higher mass velocity. Velocity in both channels remains almost constant in the single-phase region, increases slightly in the subcooled boiling region, and increases more significantly in the saturated boiling region, clearly a manifestation

of flow acceleration resulting from the axially increasing void fraction. Higher heat fluxes cause velocity to begin increasing farther upstream and more rapidly downstream, again because of the axially increasing void fraction.

4.4. Simulation and Theoretical/Empirical Predictions of Local Pressure

Pressure drop is of vital importance to the implementation of two-phase heat sinks in thermal management systems. In general, pressure drop across the heat sink is higher than those for other components of the cooling loop, save of course for the throttling valves. A higher heat sink pressure drop necessitates use of a more powerful pump and possibly thicker tubing, which would increase both power consumption and weight of the entire system.

Fig. 9 shows variations of inlet to local pressure difference ($P_{in} - P_z$) along the channel for both micro- and macro-channels at different flow rates and base heat fluxes. Shown are predictions based on both the CFD simulations and theoretical/empirical methods; different predictions for the latter are based on assumptions regarding (i) the region upstream of $x_e = 0$ (using subcooled boiling or single-phase liquid correlations) and (ii) model used for $x_e > 0$ (saturated region, HEM or SFM), as summarized in Table 6. All cases presented in Fig. 9 point to much higher pressure drop in micro-channels compared to macro-channels, a direct consequence of the much higher mass velocity and more pronounced flow acceleration in the former as shown earlier in Fig. 8.

Looking first at simulation results for the micro-channels alone, it can be seen that, for a fixed mass velocity of $G = 500$ kg/m²s,

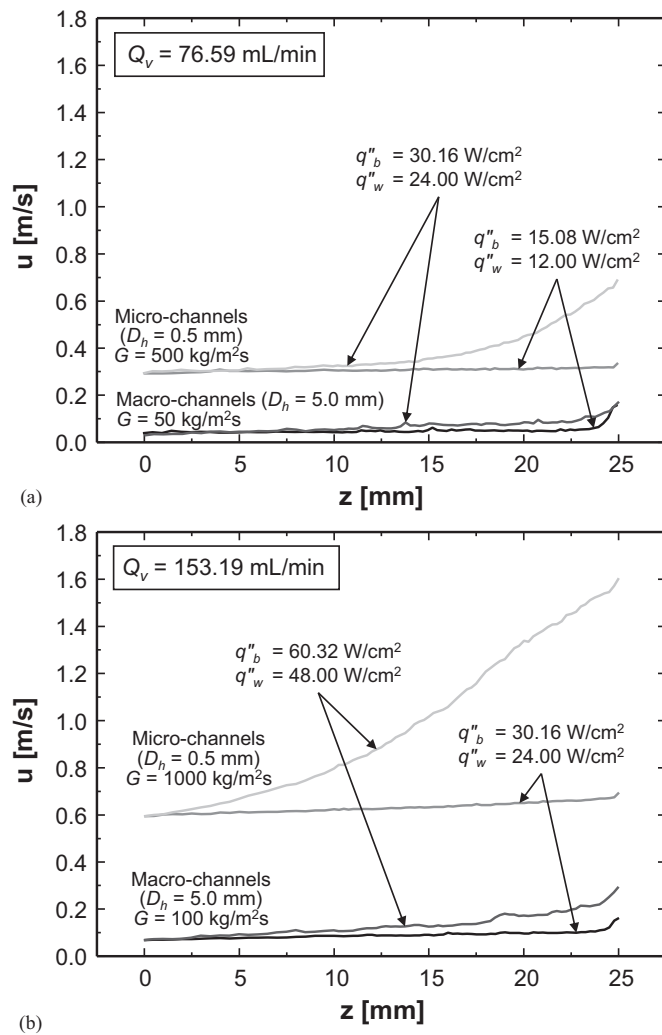


Fig. 8. Steam-wise variations of computed average fluid velocity for micro- and macrochannels at total flow rates of (a) $Q_v = 76.59$ mL/min, and (b) $Q_v = 153.19$ mL/min.

increasing the wall heat flux from $q''_w = 12$ to 24 W/cm² increases the pressure drop appreciably; this obviously is the outcome of increased vapor generation across the channel. For the same reason, the pressure drop is insignificant in the upstream, mostly single-phase liquid portion of the channel. Comparing the cases with $q''_w = 24$ W/cm² and $G = 500$ versus 1000 kg/m²s, the simulation results show great diminution in pressure drop, which can be explained by the reduction in vapor void fraction, and therefore reduced flow acceleration, with increasing G . Now comparing the cases with $G = 1000$ kg/m²s and $q''_w = 24$ versus 48 W/cm² shows an increase in pressure drop for the latter because once more of the increased void fraction. Comparing all the simulation results for micro-channels to those for macro-channels reveals similar trends except for smaller pressure drop for the latter. However, the macro-channel case corresponding to $G = 50$ kg/m²s and $q''_w = 24$ W/cm² shows an interesting trend of negligible pressure drop near the channel outlet. This can be explained by formation of an elongated bubble at the same location.

Now focusing attention on the theoretical/empirical results for the micro-channels, it is clearly seen that (i) for $x_e < 0$, using the subcooling boiling correlation yields higher pressure drop compared to using the single-phase liquid assumption, (ii) better agreement with the simulation results is achieved with the single-phase liquid assumption, (iii) theoretical/empirical predictions us-

ing HEM and SFM are fairly close to one another but reflect somewhat different trends in the saturated boiling region (as will be discussed below), and (iv) pressure drop is highest in the saturated boiling regime (this is closely related to increases in both the frictional and accelerational components of pressure drop with increasing void fraction). However, two important anomalies are captured with the theoretical/empirical models but not the simulations: (i) large downstream pressure drop escalation for $G = 1000$ kg/m²s and $q''_w = 24$ W/cm², and (ii) indication of impending two-phase choking for $G = 1000$ kg/m²s and $q''_w = 48$ W/cm². These near-choking anomalies will be discussed in more detail later. Looking now at the theoretical/empirical results for macro-channels, it is obvious there is somewhat better agreement with the simulation results compared to the micro-channels, especially when using the single-phase liquid assumption for $x_e < 0$. Overall, these results point to the ability to achieve good predictions for both channels by using the simple single-phase liquid assumption for $x_e < 0$.

For the bottommost micro-channel case, HEM predicts a negative pressure drop at around the middle of the channel. This is because of the combined effects of flashing, compressibility, and kinetic energy in the coupled momentum-energy equation. The theoretical/empirical prediction code is stopped here because further calculations kept yielding much larger negative pressure drop values, leading to divergence. On the other hand, SFM predicts very large ΔP (≈ 110 kPa), causing absolute pressure near the channel outlet to go lower than what we have properties for FC-72 (10 kPa); so, the prediction code could not proceed.

For the third micro-channel case from the top, results are obtained from three theoretical/empirical models. But the model employing subcooled boiling with HEM incurs a negative pressure drop close to the channel outlet for the same reasons mentioned above.

We now look more closely at predictions of HEM versus SFM for the saturated region ($x_e > 0$). Notice, especially for the cases of $G = 500$ kg/m²s and $q''_w = 24$ W/cm² for the micro-channels and $G = 50$ kg/m²s and $q''_w = 24$ W/cm² for the macro-channels, that HEM yields an almost linear pressure drop variation and closer agreement with simulations for lower qualities (mostly well dispersed bubbly flow), whereas SFM yields lower pressure drop than HEM for lower qualities upstream and higher pressure drop along with better agreement with simulations for higher qualities downstream (mostly somewhat separated slug flow), with cross-over between predictions occurring at a certain axial location.

The results in Fig. 9 point to two adverse manifestations in micro-channels: (i) high pressure drop, and (ii) increased likelihood of two-phase choking; the latter will be addressed in detail in later section.

4.5. Simulation and Theoretical/Empirical Predictions of Wall Temperature

Fig. 10 compares streamwise variations of wall temperature, T_w , for the micro and macro-channels at different operating conditions, predicted using the computational and theoretical/empirical methods. All cases show discontinuities in the theoretical/empirical predictions compared to more uniform simulation results. The discontinuities are simply the result of using multiple correlations for the different flow regimes, with T_w calculated after calculating the local mean fluid temperature. One advantage of the computational method is ability to account for conjugate heat transfer occurring along the wall and axial conduction within the fluid, which is not possible with the theoretical/empirical methods. This smoothens out the effects of flow regime changes on computational streamwise T_w profiles and discontinuities are not observed. Despite the discontinuities, the theoretical/empirical predictions for the micro-

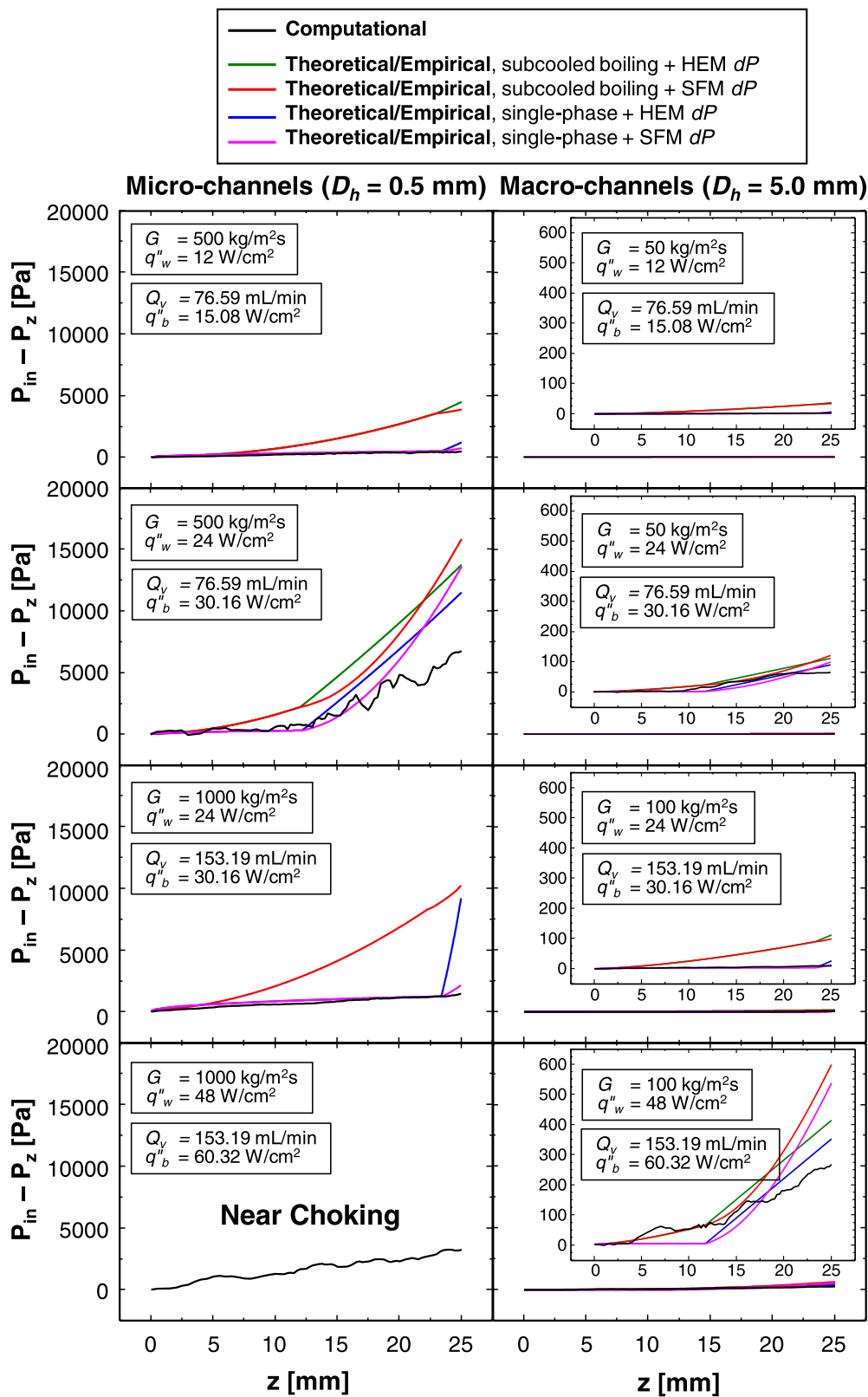


Fig. 9. Streamwise pressure drop profiles for micro- and macro-channels at different operating conditions predicted using computational and theoretical/empirical methods. Refer to Table 6 for details on the four combinations of theoretical/empirical method sub-models.

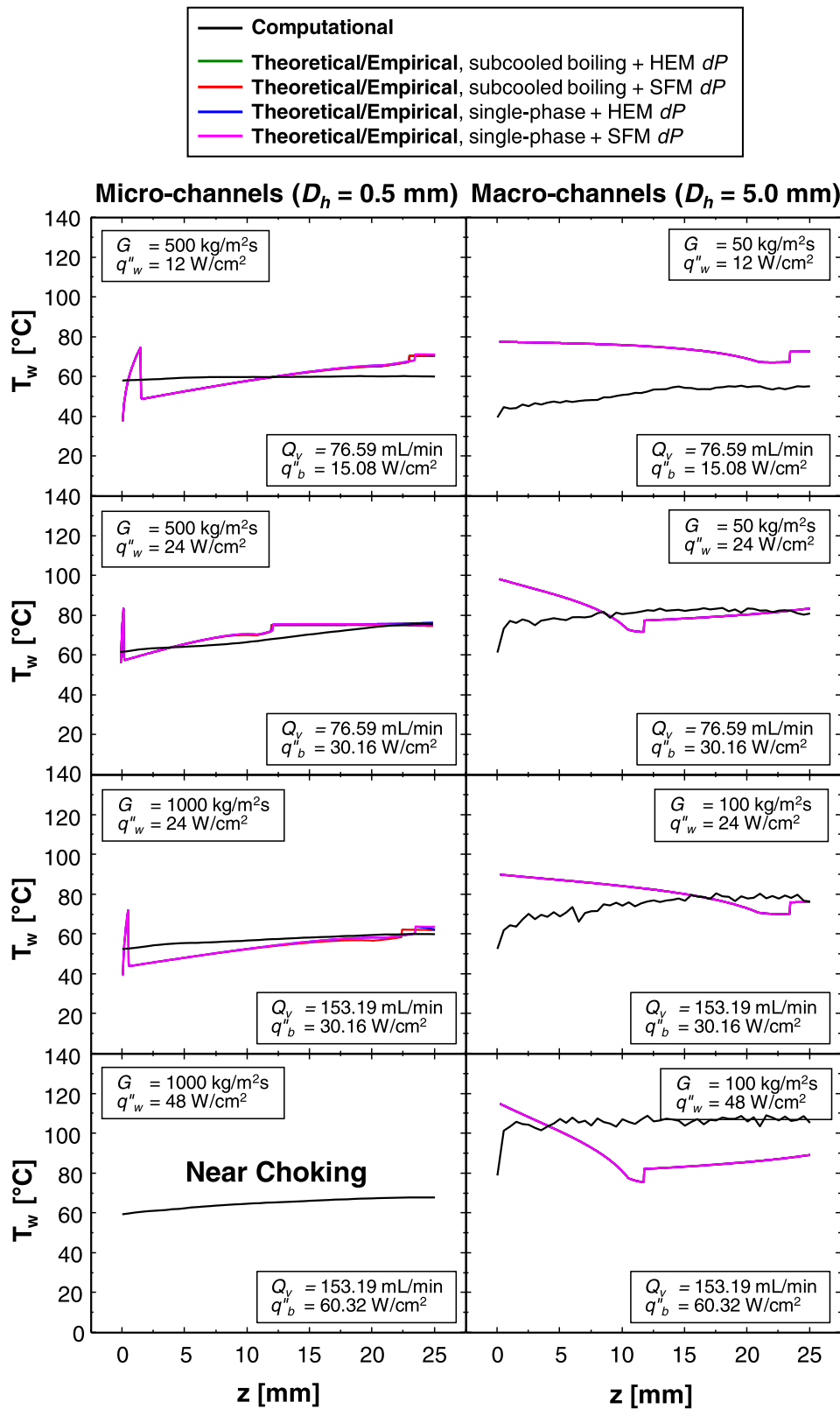


Fig. 10. Streamwise wall temperature variations for micro- and macro-channels at different operating conditions predicted using computational and theoretical/empirical methods. Refer to Table 6 for details on the four combinations of theoretical/empirical method sub-models.

channels agree fairly well with the computational results, with the best agreement achieved for the cases corresponding to $q''_w = 24$ W/cm². For the macro-channels, the computed profiles show slight fluctuations, results of larger bubbles passing close to the wall. Moreover, deviations between theoretical/empirical and simulation results are larger than those for the micro-channels.

There is a noticeable sharp rise in the theoretically/empirically predicted T_w near the micro-channel inlet followed by a sharp decrease. The initial increase is attributed to upstream sensible heating of single-phase liquid, which is interrupted a short distance downstream by ONB. As single-phase liquid is replaced by subcooled boiling, heat transfer is greatly improved, causing the observed sharp reduction in T_w . Thereafter, T_w increases axially because of a corresponding increase in the fluid temperature. Eventually, subcooled boiling is replaced by saturated boiling where fluid temperature becomes fairly constant (equal to the saturation temperature) and heat transfer coefficient a bit weaker, which culminates in an increase in T_w to a fairly constant level downstream.

The theoretically/empirically predicted wall temperature trends for the macro-channels are distinctly different. This can be explained by ONB predicted to occur very close to the inlet, i.e., the transition to subcooled boiling occurs abruptly near the inlet. Notice also that, unlike the micro-channel cases, the slope for the theoretically/empirically predicted T_w in the subcooled boiling region in macro-channels is negative, but like the micro-channels, T_w becomes fairly constant in the downstream saturated boiling region. Negative slope in the subcooled boiling region can be explained by the form of the subcooled boiling heat transfer correlation, which yields a much larger increase in subcooled boiling heat transfer coefficient towards $x_e = 0$. This large h_{sc} is higher than for micro-channels because the heat transfer enhancement of subcooled boiling over pure liquid convection is higher for flows with lower velocities (h_{sc}/h_{sp} is inversely proportional to $u_f^{0.67}$ as indicated in Table 5). This brings T_w closer to T_f at a much larger rate, making it seem as though T_w is decreasing.

It is important to comment on the apparent overlap among the theoretical/empirical models for each channel size. In reality, there are quantifiable differences among the four models, but these differences are not visible because of large limits of the vertical axis. In the saturated boiling regime, fluid temperature is set equal to T_{sat} based on local pressure, P_z . Within the relevant pressure range, T_{sat} varies little with P_z . For example, $T_{sat} = 61.73^\circ\text{C}$ at 120 kPa and 65.46°C at 135 kPa, a difference of less than 4°C . T_w is estimated using the fluid temperature by determining local heat transfer coefficient using the same subcooled and saturated boiling heat transfer correlations for all four cases (refer to Table 6). Here, the heat transfer coefficient also seems unaffected by pressure differences between the four models because fluid properties do not change appreciably over this pressure range. These facts are responsible for the apparent overlap among the four T_w curves for each channel size. Between micro- and macro-channels, the former shows larger differences in T_w due to a larger pressure drop.

5. Two-Phase Choking

5.1. Choking in Micro-Channels

Choking is an undesirable phenomenon observed in two-phase flows at high mass velocities and high heat fluxes [88]. It is manifested by a very large increase in the pressure gradient, which is the result of appreciable compressibility and flashing, the former being the outcome of specific volume variations and the latter enthalpy variations, both with respect to local pressure. Increased likelihood of two-phase choking in micro-channels was first alluded to by Bowers and Mudawar in 1994 [99] but has received limited atten-

tion in literature. Following is a summary of analytic relations governing the occurrence of choking.

5.2. Dimensionless Representation of Choking using HEM

Using the HEM, the coupled momentum-energy equation (see Table 4) indicates the key dimensionless parameters governing two-phase choking are compressibility, flashing, and, to a lesser extent, kinetic energy, which are expressed, respectively, as

$$\text{Compressibility} = G^2 \left[x_e \frac{dv_g}{dP} + (1 - x_e) \frac{dv_f}{dP} \right], \quad (11)$$

$$\text{Flashing} = \frac{G^2 v_{fg}}{h_{fg}} \left[x_e \frac{dh_g}{dP} + (1 - x_e) \frac{dh_f}{dP} \right], \quad (12)$$

and

$$\text{Kinetic Energy} = \frac{G^2 v_{fg}}{h_{fg}} [x_e v_g + (1 - x_e) v_f]. \quad (13)$$

And the choking condition is predicted using the two-phase Mach number, M , which is expressed as

$$M = \sqrt{-\frac{(\text{Compressibility} - \text{Flashing})}{(1 + \text{Kinetic Energy})}} \quad (14)$$

$$= \sqrt{-\frac{G^2 \left[x_e \frac{dv_g}{dP} + (1 - x_e) \frac{dv_f}{dP} \right] - \frac{G^2 v_{fg}}{h_{fg}} \left[x_e \frac{dh_g}{dP} + (1 - x_e) \frac{dh_f}{dP} \right]}{\left\{ 1 + \frac{G^2 v_{fg}}{h_{fg}} [x_e v_g + (1 - x_e) v_f] \right\}}}$$

Table 7 contains all properties of FC-72 and their differentials with respect to pressure required to investigate possible occurrence of choking. Table 8 provides details of all HEM choking parameters and corresponding Mach number values. Most notable is the micro-channel case with $G = 1000$ kg/m²s and $q''_w = 48$ W/cm², which is shown yielding comparatively large magnitudes for kinetic energy, compressibility, and flashing of 2311.7×10^{-5} , -27413.1×10^{-5} , 16867.6×10^{-5} , respectively, and a corresponding large Mach number of $M = 0.6626$.

Fig. 11 provides detailed variations of the three choking parameters as functions of x_e for $Q_v = 76.59$ mL/min corresponding to $G = 50$ and 500 kg/m²s for the macro- and micro-channels, respectively, and for $Q_v = 153.19$ mL/min corresponding to $G = 100$ and 1000 kg/m²s. Clearly seen is that all three terms are negligible for the macro-channels, meaning choking is highly unlikely for $D_h = 5$ mm. On the other hand, the same parameters show appreciable magnitude increases with increasing x_e for the micro-channels, especially for the higher mass velocity. Notice, for the micro-channels that values of both compressibility and flashing decrease with increasing x_e while kinetic energy follows the opposite trend. Fig. 12 shows corresponding variations of two-phase Mach number with x_e . Consistent with the values indicated in Table 8, M is appreciable only for the micro-channels, and increases with increases in both x_e and G .

5.3. Critical Flow Predictions using Homogeneous Frozen Model (HFM)

Despite the simplicity and analytical appeal of HEM, a recent article by Kim and Mudawar [100], who examined all available HEM and SFM formulations of critical flow, showed best predictions are achieved with the aid of the rather simple Homogenous Frozen Model (HFM), in which critical mass velocity, G_c , corresponding to choked flow is expressed as [101],

$$G_c = \left\{ - \left[x_e \frac{dv_g}{dP} + (1 - x_e) \frac{dv_f}{dP} \right] \right\}^{-0.5}. \quad (15)$$

Table 7
FC-72 properties and their differentials with respect to pressure at $P_{sat} = 120$ kPa.

P (N/m ²)	v_g (m ³ /kg)	dv_g/dP (m ⁵ /kg.N)	v_f (m ³ /kg)	dv_f/dP (m ⁵ /kg.N)	v_{fg} (m ³ /kg)	dv_{fg}/dP (m ⁵ /kg.N)	h_g (J/kg)	dh_g/dP (m ³ /kg)	h_f (J/kg)	dh_f/dP (m ³ /kg)	h_{fg} (J/kg)	dh_{fg}/dP (m ³ /kg)
1.200×10^5	0.06356	-5.141×10^{-7}	6.334×10^{-4}	2.678×10^{-10}	0.06293	-5.143×10^{-7}	1.947×10^5	0.2107	1.016×10^5	0.2941	9.311×10^4	-0.08339

Table 8
HEM choking parameters for micro- and macro-channels, calculated at $P_{sat} = 120$ kPa.

Channel	G (kg/m ² s)	q''_w (W/cm ²)	$x_{e,out}$	Kinetic energy $\times 10^5$	Compressibility $\times 10^5$	Flashing $\times 10^5$	M
Micro-channel, $D_h = 0.5$ mm	500	12	0.0180	29.84913	-224.882	4942.99	0.2273
	500	24	0.5335	577.9258	-6853.28	4216.892	0.3324
	1000	24	0.0180	119.3965	-899.528	19771.96	0.4544
	1000	48	0.5335	2311.703	-27413.1	16867.57	0.6626
Macro-channel, $D_h = 5$ mm	50	12	0.0180	0.298491	-2.24882	49.4299	0.0227
	50	24	0.5335	5.779258	-68.5328	42.16892	0.0333
	100	24	0.0180	1.193965	-8.99528	197.7196	0.0455
	100	48	0.5335	23.11703	-274.131	168.6757	0.0665

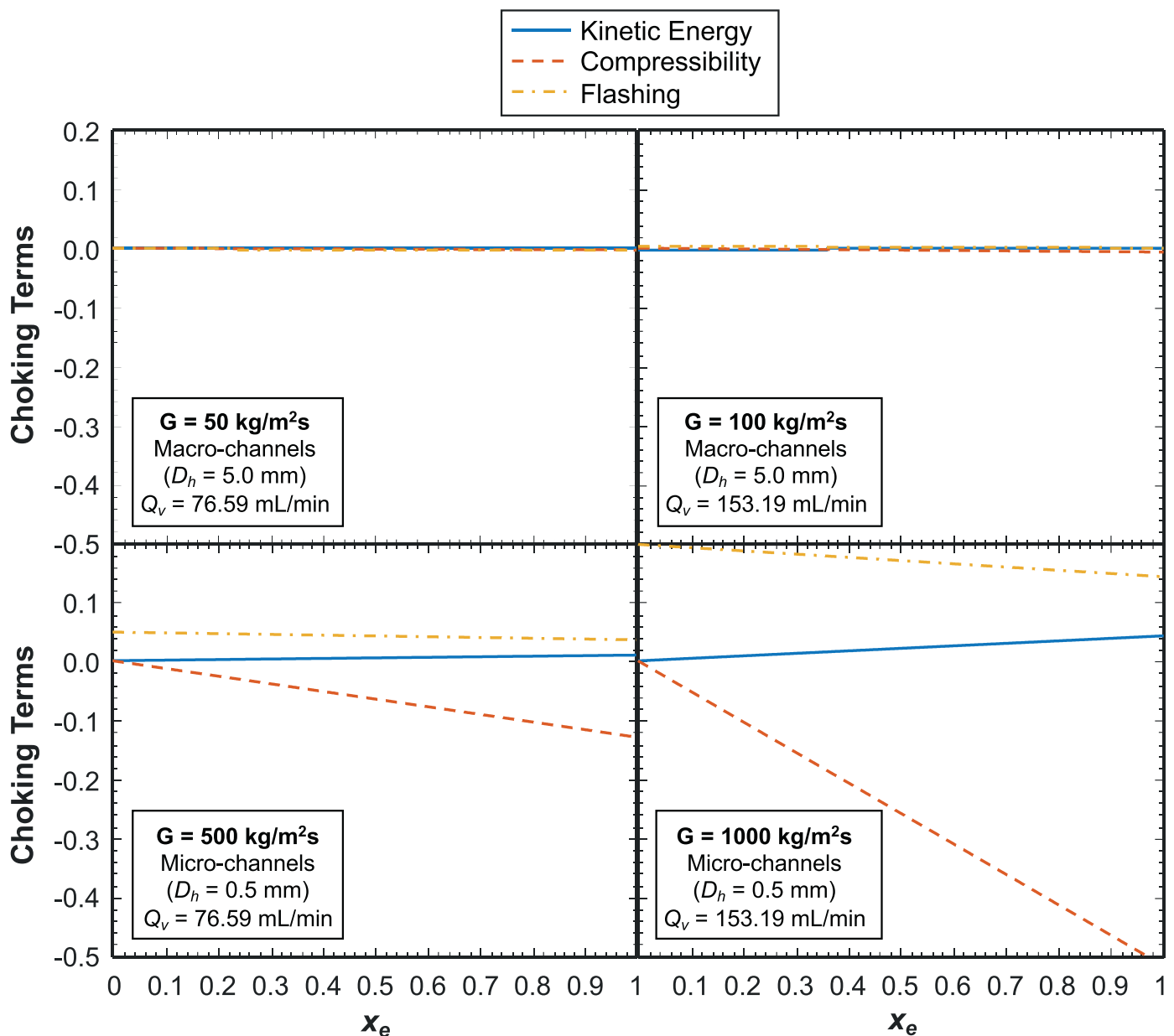


Fig. 11. Variations of kinetic energy, compressibility, and flashing terms with thermodynamic equilibrium quality for micro- and macro-channels for $P_{sat} = 120$ kPa and flow rates of $Q_v = 76.59$ and 153.19 mL/min.

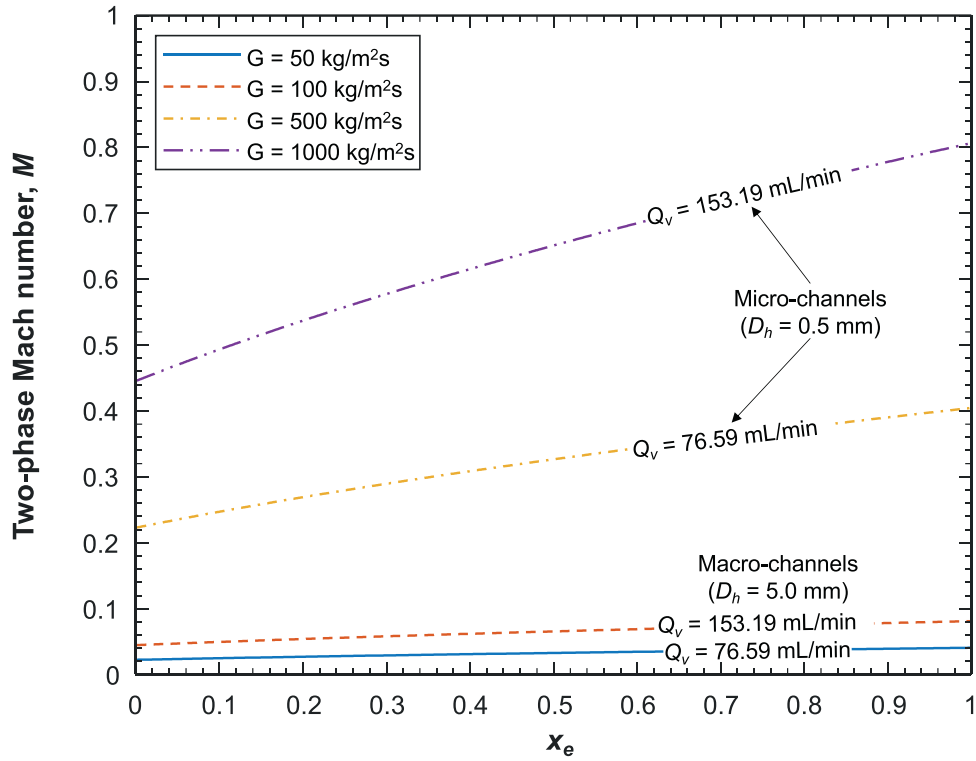


Fig. 12. Variations of two-phase Mach number with thermodynamic equilibrium quality for micro- and macrochannels for $P_{sat} = 120 \text{ kPa}$ and flow rates of $Q_v = 76.59$ and 153.19 mL/min .

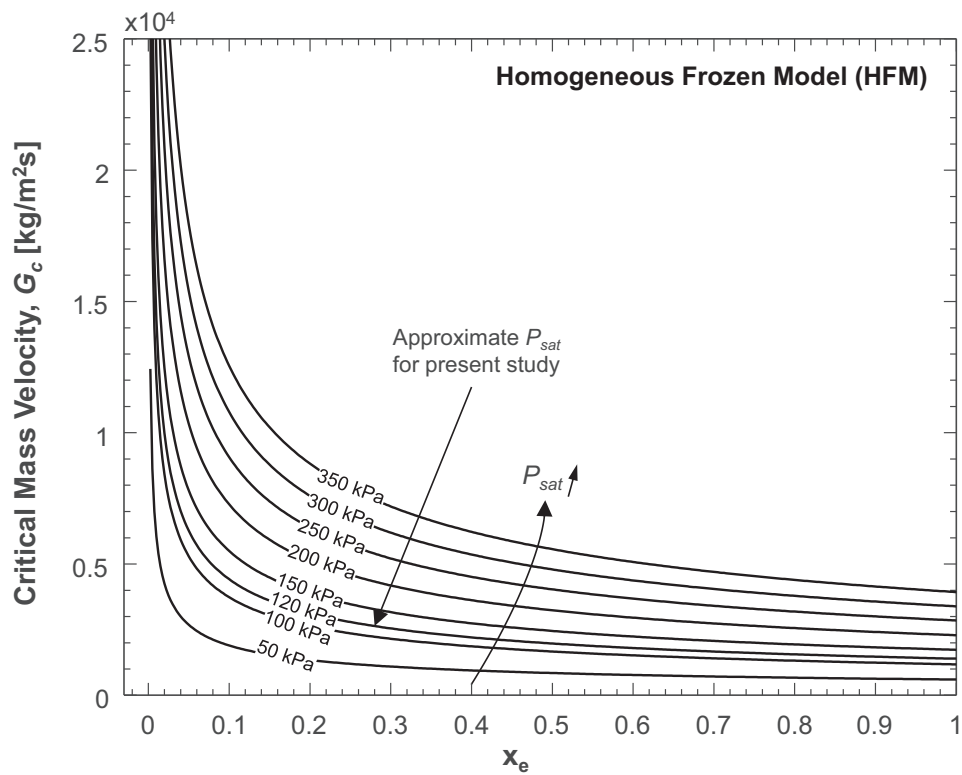


Fig. 13. Variations of critical mass velocity for FC-72 with thermodynamic quality for different pressures, predicted using the Homogeneous Frozen Model (HFM).

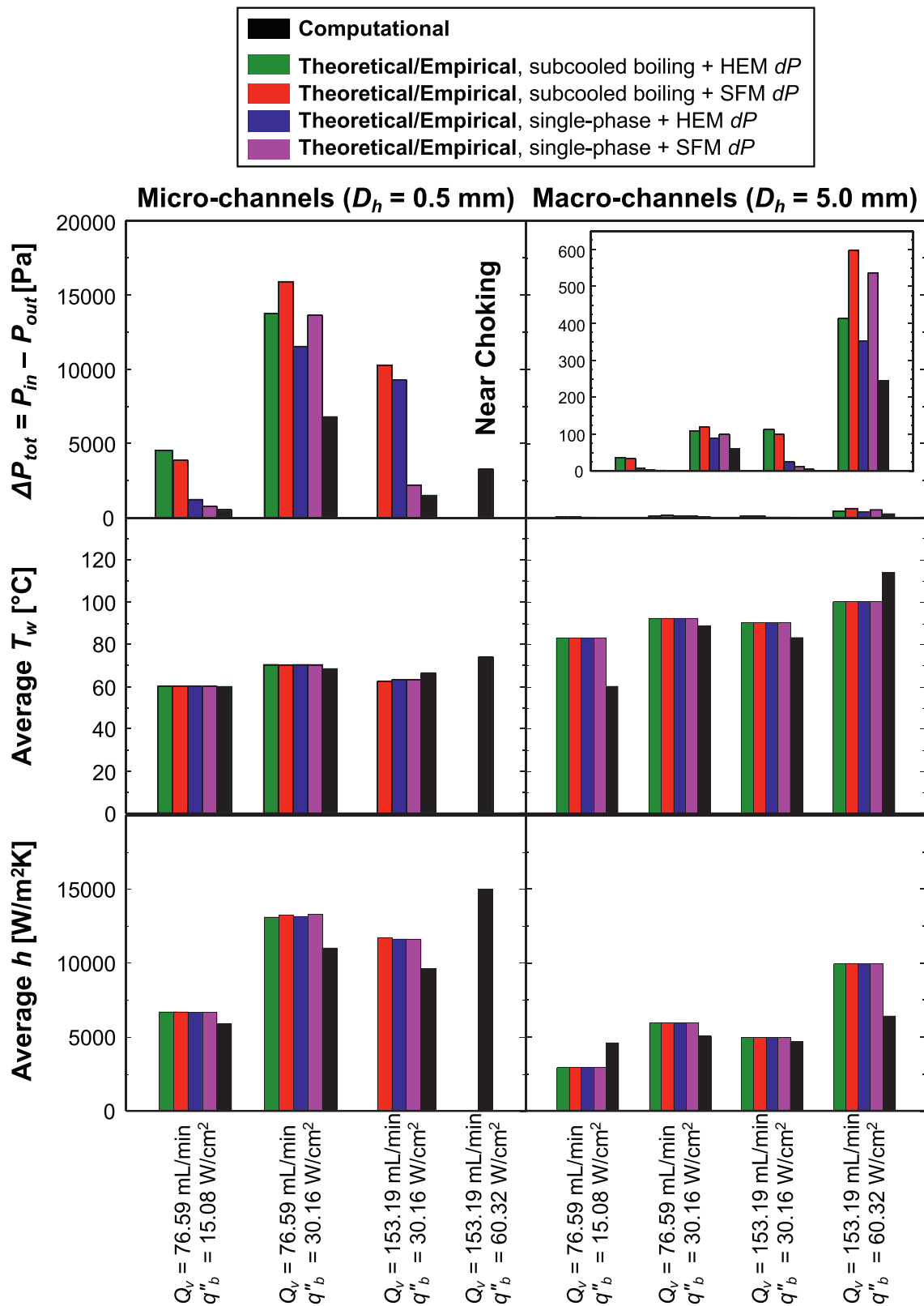


Fig. 14. Comparison of computational and theoretical/empirical predictions of total pressure, drop, average wall temperature, and average heat transfer coefficient for micro- and macro-channel heat sinks at different operating conditions. Refer to Table 6 for details on the four combinations of theoretical/empirical method sub-models.

Table 9
Critical mass velocity predicted according to the Homogenous Frozen Model (HFM) for micro- and macro-channels, calculated at $P_{sat} = 120$ kPa.

Channel	G (kg/m ² s)	q''_w (W/cm ²)	$x_{e,out}$	$G_{c,HFM}$ (kg/m ² s)
Micro-channel, $D_h = 0.5$ mm	500	12	0.0180	10543.69
	500	24	0.5335	1909.94
	1000	24	0.0180	10543.69
	1000	48	0.5335	1909.94
Macro-channel, $D_h = 5$ mm	50	12	0.0180	10543.69
	50	24	0.5335	1909.94
	100	24	0.0180	10543.69
	100	48	0.5335	1909.94

It is evident from Eq. (15) that G_c is a function of thermodynamic equilibrium quality, fluid properties, and saturation pressure. Fig. 13 shows variations of G_c for FC-72 as a function of x_e for different pressures. For a fixed x_e , G_c is shown increasing monotonically with increasing P_{sat} , which implies higher pressure allows the two-phase channel flow to accommodate higher flow rates before choking. And, for a fixed P_{sat} , G_c decreases monotonically with increasing x_e , the rate of decrease being steeper for low quality values and milder for high values. Notice the very high G_c values as x_e approaching zero. This is the outcome of a singularity when using Eq. (15).

Table 9 provides values of G_c for all cases of the present study, which are based on outlet quality, $x_{e,out}$, and $P_{sat} = 120$ kPa. The likelihood of choking for each case is assessed by comparing G_c to the corresponding mass velocity, G . The lowest G_c value predicted by the HFM is 1909.9 kg/m²s. Of the eight cases considered, the lowest G_c is closest to G for micro-channels with the highest mass velocity of $G = 1000$ kg/m²s and $q''_w = 48$ W/cm², which is consistent with both the theoretical/empirical results for pressure drop shown earlier in Fig. 9, and the highest two-phase Mach number case in Table 8, which was predicted using HEM. Clearly, this particular case points to conditions approaching choking and must therefore be concerning from a thermal management point of view. On the other hand, Table 9 shows G_c values for macro-channels are far greater than those of G for all macro-channel cases. The main inference here is that micro-channels are prone to choking while macro-channels are not, which also means flow boiling in micro-channels must be carefully assessed for possible occurrence of choking.

Notice in Fig. 9 how the two micro-channel cases corresponding to $G = 1000$ kg/m²s and $q''_w = 24$ and 48 W/cm² are predicted by the theoretical/empirical models to approach choking, more closely so for the higher heat flux, where appreciable compressibility and flashing effects are incurred around the middle of the channel. On the other hand, for the lower heat flux, a sharp increase in pressure drop is localized near the outlet because of mostly strong flashing effects.

It is useful to tie near-choking conditions to interfacial behavior captured earlier in the computed flow pattern plots, Fig. 7. Notice for the most concerning micro-channel case corresponding to $G = 1000$ kg/m²s and $q''_w = 48$ W/cm², Fig. 7(d), the presence of a large and distorted long vapor bubble filling the entire cross-section of the channel. This clearly points to high vapor quality values and correspondingly high computed pressure drop as shown in Fig. 9. But, while the simulations might provide indication of tendency for choking, they do not provide a precise means for capturing choking conditions as HEM and HFM models do.

6. Overall Performance Comparison of Micro- and Macro-channel Heat Sinks

After assessing performances of the micro- and macro-channel heat sinks relative to individual parameters, it is useful to conclude

the study by providing an overall assessment of the advantages and disadvantages of each. Fig. 14 shows comparisons of computational and theoretical/empirical predictions for total pressure drop (from inlet to outlet), average wall temperature (over entire channel length), and average heat transfer coefficient (over entire channel length) for both channels and different operating conditions.

In terms of predictive capability, the computational and theoretical/empirical methods show excellent agreement in predicting average wall temperatures and good agreement in average heat transfer coefficients for both channels, evidenced by respective Mean Absolute Errors (MAEs) of 8.91% and 22.41% (calculated as computational against theoretical/empirical predictions). It is noted that the consolidated theoretical/empirical methods comprise widely-accepted models and correlations that have been validated against large experimental databases by numerous researchers. The worst deviation in the heat transfer predictions is seen in the case of macro-channels with $G = 50$ kg/m²s and $q''_w = 12$ W/cm², where computed average T_w and average h values are, respectively, 27.55% lower and 55.29% higher than theoretical/empirical predictions. As to total pressure drop, ΔP , simulations underpredict the theoretical/empirical methods for both channels; best agreement between the two methods is achieved with the theoretical/empirical methods utilizing the assumption of single-phase liquid flow up to $x_e = 0$. As to the saturated boiling pressure drop model, better similitude is achieved by SFM for cases with a lower exit quality of 0.018 (both $Q_v = 76.59$ mL/min at $q''_b = 15.08$ W/cm² and $Q_v = 153.19$ mL/min at $q''_b = 30.16$ W/cm²), and HEM for cases with a higher exit quality of 0.534 (both $Q_v = 76.59$ mL/min at $q''_b = 30.16$ W/cm² and $Q_v = 153.19$ mL/min at $q''_b = 60.32$ W/cm²). This is due to the different stream-wise pressure drop profile trends discussed in section 4.4.

But the main outcome of the study is identifying key advantages and disadvantages of each channel. Overall,

- (1) Compared to macro-channels, micro-channels offer significantly better heat transfer performance, reflected by both higher average heat transfer coefficients and lower average wall temperatures.
- (2) Compared to macro-channels, micro-channels suffer significantly higher pressure drop, in addition of much higher likelihood of two-phase choking.

7. Conclusions

This study focused on assessing the advantages and disadvantages of micro- and macro-channel flow boiling for high-heat-flux thermal management using both computational and theoretical/empirical methods. Computational simulations of subcooled FC-72 flow boiling along an entire channel representing a multi-channel heat sink were conducted in ANSYS FLUENT by adopting the multi-phase VOF method, the Lee phase change model, and accounting for both shear lift force and conjugated wall heat transfer. Computational results for both channels operating at different flow

rates and heat fluxes were compared with analytical results obtained using the Homogeneous Equilibrium Model (HEM) and Separated Flow Model (SFM). Finally, both HEM and the Homogeneous Frozen Model (HFM) are used to assess the likelihood of two-phase choking. Key conclusions from the study are as follows:

- (1) CFD determined steady state flow patterns indicate that vapor bubbles in micro-channels tend to first fill the flow area before growing in the axial direction. On the other hand, macro-channels can accommodate a higher number of large bubbles which show little confinement or tendency for axial elongation. Overall, bubble shapes are more distorted at higher mass velocities. Interfacial features are fairly symmetrical about the central axis, with a slight asymmetry resulting from both randomness in bubble production at the wall and small-scale turbulence effects.
- (2) The two-phase mixture accelerates along the flow direction because of increasing vapor production, and the acceleration is more pronounced with increases in both flow rate and local void fraction.
- (3) Larger pressure drop is observed in micro-channels compared to negligibly small values in macro-channels. CFD simulations yield pressure profile trends similar to those of the theoretical/empirical methods. For the theoretical/empirical methods, better agreement with the simulations is achieved when using the simple assumption of single-phase liquid flow from the inlet to the axial location corresponding to $x_e = 0$.
- (4) Streamwise wall temperature profiles predicted by the two methods show good overall agreement except for macro-channels at low mass velocity and low heat flux. Computational profiles are smoothed out by allowance of axial heat conduction through the fluid and wall, and conjugated heat transfer effects in the wall.
- (5) Micro-channels at $G = 1000 \text{ kg/m}^2\text{s}$ and $q''_w = 24$ and 48 W/cm^2 are predicted by the theoretical/empirical methods to approach choking. For $q''_w = 48 \text{ W/cm}^2$, HEM predicts an adverse pressure gradient at around the middle of the channel due to strong compressibility and flashing effects. For the same heat flux, both HEM and SFM point to a tendency for choking, evidenced by a two-phase Mach number approaching unity.
- (6) Overall, micro-channel heat sinks offer better heat transfer performance with higher heat transfer coefficients and lower wall temperatures. But this comes at the cost of significantly higher pressure drop and pumping power requirements. Micro-channels are also prone to choking due to high two-phase Mach numbers.

Declaration of Competing Interest

None. The authors declare that they have no known competing financial interests or personal relationships that could have appeared to influence the work reported in this paper.

Acknowledgements

The authors are grateful for the financial support provided by the China Scholarship Council (No. 201806090046) and Scientific Research Foundation of Graduate School of Southeast University (No. YBJJ1804).

References

- [1] I. Mudawar, Assessment of high heat flux thermal management schemes, *IEEE Trans. Compon. Packag. Technol.* 24 (2001) 122–141.
- [2] I. Mudawar, Recent advances in high-flux, two-phase thermal management, *J. Therm. Sci. Eng. Appl.* 5 (2013) 021012.
- [3] H. Zhang, I. Mudawar, Experimental and theoretical study of orientation effects on flow boiling CHF, *Int. J. Heat Mass Transfer* 45 (2002) 4463–4477.
- [4] C. Konishi, I. Mudawar, Review of flow boiling and critical heat flux in microgravity, *Int. J. Heat Mass Transfer* 80 (2015) 469–493.
- [5] T.J. LaClair, I. Mudawar, Thermal transients in a capillary evaporator prior to the initiation of boiling, *Int. J. Heat Mass Transfer* 43 (2000) 3937–3952.
- [6] T.M. Anderson, I. Mudawar, Parametric investigation into the effects of pressure, subcooling, surface augmentation and choice of coolant on pool boiling in the design of cooling systems for high-power density chips, *J. Electron. Packag.* 112 (1990) 375–382.
- [7] I. Mudawar, T.M. Anderson, Optimization of enhanced surfaces for high flux chip cooling by pool boiling, *J. Electron. Packag.* 115 (1993) 89–100.
- [8] I. Mudawar, R.A. Houpt, Mass and momentum transport in smooth falling liquid films laminarized at relatively high Reynolds numbers, *Int. J. Heat Mass Transfer* 36 (1993) 3437–3448.
- [9] C.O. Gersey, I. Mudawar, Effects of heater length and orientation on the trigger mechanism for near-saturated flow boiling CHF - I. Photographic and statistical characterization of the near-wall interfacial features, *Int. J. Heat Mass Transfer* 38 (1995) 629–642.
- [10] S. Mukherjee, I. Mudawar, Smart, low-cost, pumpless loop for micro-channel electronic cooling using flat and enhanced surfaces, in: 8th Intersoc. Conf. Therm. Thermomech. Phenom. Electron. Syst., IEEE (2002) 360–370.
- [11] J. Lee, I. Mudawar, Critical heat flux for subcooled flow boiling in micro-channel heat sinks, *Int. J. Heat Mass Transfer* 52 (2009) 3341–3352.
- [12] M.E. Johns, I. Mudawar, An ultra-high power two-phase jet-impingement avionic clamshell module, *J. Electron. Packag.* 118 (1996) 264–270.
- [13] W.P. Klinzing, J.C. Rozzi, Film and transition boiling correlations for quenching of hot surfaces with water sprays, *J. Heat Treating* 9 (1992) 91–103.
- [14] M.K. Sung, I. Mudawar, Single-phase and two-phase heat transfer characteristics of low temperature hybrid micro-channel/micro-jet impingement cooling module, *Int. J. Heat Mass Transfer* 51 (2008) 3882–3895.
- [15] I. Mudawar, Two-phase microchannel heat sinks: theory, applications, and limitations, *J. Electron. Packag.* 133 (2011) 041002.
- [16] P.A. Kew, K. Cornwell, Correlations for the prediction of boiling heat transfer in small-diameter channels, *Appl. Therm. Eng.* 17 (1997) 705–715.
- [17] S.S. Mehendale, A.M. Jacob, R.K. Shah, Fluid flow and heat transfer at micro- and meso-scales with application to heat exchanger design, *Appl. Mech. Rev.* 53 (2000) 175–193.
- [18] L. Friedel, Improved friction pressure drop correlations for horizontal and vertical two-phase pipe flow, *European Two-Phase Group Meeting* (1979) Paper E2.
- [19] H. Müller-Steinhagen, K. Heck, A simple friction pressure drop correlation for two-phase flow in pipes, *Chem. Eng. Proc.* 20 (1986) 297–308.
- [20] L. Sun, K. Mishima, Evaluation analysis of prediction methods for two-phase flow pressure drop in mini-channels, *Int. J. Multiphase Flow* 35 (2009) 47–54.
- [21] W. Zhang, T. Hibiki, K. Mishima, Correlations of two-phase frictional pressure drop and void fraction in mini-channel, *Int. J. Heat Mass Transfer* 53 (2010) 453–465.
- [22] W. Li, Z. Wu, A general correlation for adiabatic two-phase pressure drop in micro/mini-channels, *Int. J. Heat Mass Transfer* 53 (2010) 2732–2739.
- [23] W. Li, Z. Wu, Generalized adiabatic pressure drop correlations in evaporative micro/mini-channels, *Exp. Therm. Fluid Sci.* 35 (2011) 866–872.
- [24] K.E. Gungor, R.H.S. Winterton, A general correlation for flow boiling in tubes and annuli, *Int. J. Heat Mass Transfer* 29 (1986) 351–358.
- [25] Z. Liu, R.H.S. Winterton, A general correlation for saturated and subcooled flow boiling in tubes and annuli, based on a nucleate pool boiling equation, *Int. J. Heat Mass Transfer* 34 (1991) 2759–2766.
- [26] W. Li, Z. Wu, A general correlation for evaporative heat transfer in micro/mini-channels, *Int. J. Heat Mass Transfer* 53 (2010) 1778–1787.
- [27] S.M. Kim, I. Mudawar, Universal approach to predicting two-phase frictional pressure drop for adiabatic and condensing mini/micro-channel flows, *Int. J. Heat Mass Transfer* 55 (2012) 3246–3261.
- [28] S.M. Kim, I. Mudawar, Universal approach to predicting saturated flow boiling heat transfer in mini/micro-channels - Part I. Dryout incipience quality, *Int. J. Heat Mass Transfer* 64 (2013) 1226–1238.
- [29] S.M. Kim, I. Mudawar, Universal approach to predicting saturated flow boiling heat transfer in mini/micro-channels - Part II. Two-phase heat transfer coefficient, *Int. J. Heat Mass Transfer* 64 (2013) 1239–1256.
- [30] S.M. Kim, I. Mudawar, Theoretical model for annular flow condensation in rectangular micro-channels, *Int. J. Heat Mass Transfer* 55 (2012) 958–970.
- [31] S.M. Kim, I. Mudawar, Theoretical model for local heat transfer coefficient for annular flow boiling in circular mini/micro-channels, *Int. J. Heat Mass Transfer* 73 (2014) 731–742.
- [32] C.R. Kharangate, I. Mudawar, Review of computational studies on boiling and condensation, *Int. J. Heat Mass Transfer* 108 (2017) 1164–1196.
- [33] S. Jeon, S. Kim, G. Park, Numerical study of condensing bubble in subcooled boiling flow using volume of fluid model, *Chem. Eng. Sci.* 66 (2011) 5899–5909.
- [34] M. Magnini, B. Pulvirenti, J.R. Thome, Numerical investigation of hydrodynamics and heat transfer of elongated bubbles during flow boiling in a microchannel, *Int. J. Heat Mass Transfer* 59 (2013) 451–471.
- [35] M. Bahreini, A. Ramiar, A.A. Ranjbar, Numerical simulation of bubble behavior in subcooled flow boiling under velocity and temperature gradient, *Nucl. Eng. Des.* 293 (2015) 238–248.
- [36] R. Zhuan, W. Wang, Simulation on nucleate boiling in micro-channel, *Int. J. Heat Mass Transfer* 53 (2010) 502–512.

- [37] Y.Q. Zu, Y.Y. Yan, S. Gedupudi, T.G. Karayiannis, D.B.R. Kenning, Confined bubble growth during flow boiling in a mini-/micro-channel of rectangular cross-section part II: approximate 3-D numerical simulation, *Int. J. Therm. Sci.* 5 (2011) 267–273.
- [38] D.L. Youngs, K.W. Morton, M.L. Norman (Eds.), *Time-dependent multi-material flow with large fluid distribution* (1986) 187–221.
- [39] E. Shirani, N. Ashgriz, J. Mostaghimi, Interface pressure calculation based on conservation of momentum for front capturing methods, *J. Comput. Phys.* 203 (2005) 154–175.
- [40] D. Lörstäd, L. Fuchs, High-order surface tension VOF-model for 3D bubble flows with high density ratio, *J. Comput. Phys.* 200 (2004) 153–176.
- [41] F. Dong, Z. Wang, T. Cao, J. Ni, A novel interphase mass transfer model toward the VOF simulation of subcooled flow boiling, *Numer. Heat Transfer, Part A* 76 (2019) 220–231.
- [42] F. Gibou, L. Chen, D. Nguyen, S. Banerjee, A level set based sharp interface method for the multiphase incompressible Navier-Stokes equations with phase change, *J. Comput. Phys.* 222 (2007) 536–555.
- [43] R.W. Schrage, *A Theoretical Study of Interface Mass Transfer*, Columbia Univ. Press, New York, NY, USA, 1953 0.
- [44] W.H. Lee, Pressure iteration scheme for two-phase flow modeling, *Multi-Phase Transport: Fundamentals, Reactor Safety, Appl* 1 (1980) 407–431.
- [45] B.A. Nichita, J.R. Thome, A level set method and a heat transfer model implemented into FLUENT for modeling of microscale two phase flows, AVT-178 Specialists' Meeting on System Level Thermal Management for Enhanced Platform Efficiency, Bucharest, Romania, 2010.
- [46] D.L. Sun, J.L. Xu, L. Wang, Development of a vapor-liquid phase change model for volume-of-fluid method in FLUENT, *Int. Commun. Heat Mass Transfer* 39 (2012) 1101–1106.
- [47] Y.S. Huang, Heat transfer by condensation of low pressure metal vapors, Case Western Reserve Univ., Cleveland, Ohio, USA, 1971 Ph.D. Thesis.
- [48] G.S. Springer, A.J. Patton, A kinetic theory description of liquid-vapor phase change, in: *Proc. 6th Int. Symp. Rarefied Gas Dynamics*, 1969, p. 1497.
- [49] D.A. Labuntzov, A.P. Kryukov, Analysis of intensive evaporation and condensation, *Int. J. Heat Mass Transfer* 22 (1979) 989–1002.
- [50] S. Chen, Z. Yang, Y. Duan, Y. Chen, D. Wu, Simulation of condensation flow in a rectangular microchannel, *Chem. Eng. Process. Process Intensif.* 76 (2014) 60–69.
- [51] L. Pan, Z. Tan, D. Chen, L. Xue, Numerical investigation of vapor bubble condensation characteristics of subcooled flow boiling in vertical rectangular channel, *Nucl. Eng. Des.* 248 (2012) 126–136.
- [52] M. Bahreini, A. Ramiar, A.A. Ranjbar, Numerical simulation of subcooled flow boiling under conjugate heat transfer and microgravity condition in a vertical mini channel, *Appl. Therm. Eng.* 113 (2017) 170–185.
- [53] S.R.G. Vadlamudi, A.K. Nayak, CFD simulation of departure from nucleate boiling in vertical tubes under high pressure and high flow conditions, *Nucl. Eng. Des.* 352 (2019).
- [54] J. Lee, L.E. O'Neill, S. Lee, I. Mudawar, Experimental and computational investigation on two-phase flow and heat transfer of highly subcooled flow boiling in vertical upflow, *Int. J. Heat Mass Transfer* 136 (2019) 1199–1216.
- [55] J. Lee, L.E. O'Neill, I. Mudawar, 3-D computational investigation and experimental validation of effect of shear-lift on two-phase flow and heat transfer characteristics of highly subcooled flow boiling in vertical upflow, *Int. J. Heat Mass Transfer* 150 (2020) 119291.
- [56] W. Lee, G. Son, Bubble dynamics and heat transfer during nucleate boiling in a microchannel, *Numer. Heat Transfer, Part A* 53 (2008) 1074–1090.
- [57] Y. Suh, W. Lee, G. Son, Bubble dynamics, flow, and heat transfer during flow boiling in parallel microchannels, *Numer. Heat Transfer, Part A* 54 (2008) 390–405.
- [58] A. Mukherjee, Contribution of thin-film evaporation during flow boiling inside microchannels, *Int. J. Therm. Sci.* 48 (2009) 2025–2035.
- [59] R. Zhuan, W. Wang, Simulation of subcooled flow boiling in a micro-channel, *Int. J. Refrig.* 34 (2011) 781–795.
- [60] J. Wei, L. Pan, D. Chen, H. Zhang, J. Xu, Y. Huang, Numerical simulation of bubble behaviors in subcooled flow boiling under swing motion, *Nucl. Eng. Des.* 241 (2011) 2898–2908.
- [61] M. Magnini, B. Pulvirenti, J.R. Thome, Numerical investigation of the influence of leading and sequential bubbles on slug flow boiling within a microchannel, *Int. J. Therm. Sci.* 71 (2013) 36–52.
- [62] M. Magnini, J.R. Thome, Computational study of saturated flow boiling within a microchannel in the slug flow regime, *J. Heat Transfer* 138 (2016) 021502.
- [63] S. Zhou, X. Xu, B.G. Sammakia, Modeling of boiling flow in microchannels for nucleation characteristics and performance optimization, *Int. J. Heat Mass Transfer* 64 (2013) 706–718.
- [64] D. Lorenzini, Y.K. Joshi, CFD analysis of flow boiling in a silicon microchannel with non-uniform heat flux, in: *Proc. ASME 2015 13th Int. Conf. on Nanochannels, Microchannels, and Minichannels*, San Francisco, California, USA, 2015.
- [65] Q. Liu, W. Wang, B. Palm, Numerical study of the interactions and merge of multiple bubbles during convective boiling in micro channels, *Int. Commun. Heat Mass Transfer* 80 (2017) 10–17.
- [66] J. Kim, J.S. Lee, Numerical study on the effects of inertia and wettability on subcooled flow boiling in microchannels, *Appl. Therm. Eng.* 152 (2019) 175–183.
- [67] R. Zhuan, W. Wang, Flow pattern of boiling in micro-channel by numerical simulation, *Int. J. Heat Mass Transfer* 55 (2012) 1741–1753.
- [68] ANSYS FLUENT 15.0 in Workbench User's Guide, ANSYS Inc., Canonsburg, PA, USA, 2013.
- [69] B. Lafaurie, C. Nardone, R. Scardovelli, S. Zaleski, G. Zanetti, Modelling merging and fragmentation in multiphase flows with SURFER, *J. Comput. Phys.* 113 (1994) 134–147.
- [70] F.R. Menter, Two-equation eddy-viscosity turbulence models for engineering applications, *AIAA J* 32 (1994) 1598–1605.
- [71] Y.C. Lei, I. Mudawar, Z.Q. Chen, Computational and experimental investigation of condensation flow patterns and heat transfer in parallel rectangular micro-channels, *Int. J. Heat Mass Transfer* 149 (2020) 119158.
- [72] F.H. Harlow, A.A. Amsden, Flow of interpenetrating material phases, *J. Comp. Physics* 18 (1975) 440–464.
- [73] S.A. Hosseini, R. Kouhikamali, A numerical investigation of various phase change models on simulation of saturated film boiling heat transfer, *Heat Transfer Asian Res* 48 (2019) 2577–2595.
- [74] J.F. R.K. Mei, Shear lift force on spherical bubbles, *J. Fluid Mech.* 183 (1987) 190–218.
- [75] P.G. Saffman, The lift on a small sphere in a slow shear flow, *J. Fluid Mech.* 22 (1965) 385–400.
- [76] T.R. Auton, The lift force on a spherical body in a rotational flow, *J. Fluid Mech.* 183 (1987) 199–218.
- [77] X. Yin, Y. Tian, D. Zhou, N. Wang, Numerical study of flow boiling in an intermediate-scale vertical tube under low heat flux, *Appl. Therm. Eng.* 153 (2019) 739–747.
- [78] GAMBIT 2.2.30 User's Guide, ANSYS Inc., Canonsburg, PA, USA, 2005.
- [79] E.W. Lemmon, M.L. Huber, M.O. McLinden, NIST Standard Reference Database 23: Reference Fluid Thermodynamic and Transport Properties-REFPROP, Version 9.0 (2010) Standard Reference Data Program.
- [80] S.M. Kim, I. Mudawar, Consolidated method to predicting pressure drop and heat transfer coefficient for both subcooled and saturated flow boiling in micro-channel heat sinks, *Int. J. Heat Mass Transfer* 55 (2012) 3720–3731.
- [81] S. Lee, V.S. Devahdhanush, I. Mudawar, Investigation of subcooled and saturated boiling heat transfer mechanisms, instabilities, and transient flow regime maps for large length-to-diameter ratio micro-channel heat sinks, *Int. J. Heat Mass Transfer* 123 (2018) 172–191.
- [82] S. Lee, V.S. Devahdhanush, I. Mudawar, Frequency analysis of pressure oscillations in large length-to-diameter two-phase micro-channel heat sinks, *Int. J. Heat Mass Transfer* 116 (2018) 273–291.
- [83] T. Sato, H. Matsumura, On the conditions of incipient subcooled-boiling with forced convection, *Bull. JSME* 7 (1963) 392–398.
- [84] S.W. Churchill, R. Usagi, A general expression for the correlation of rates of transfer and other phenomena, *AIChE J* 18 (1972) 1121–1128.
- [85] D. Copeland, Manifold microchannel heat sinks: analysis and optimization, in: *Proc. ASME-JSME Therm. Eng. Joint Conf.*, 4, 1995, pp. 169–174. 1995.
- [86] W. Zhi-qing, Study on correction coefficients of laminar and turbulent entrance region effect in round pipe, *Appl. Math. Mech.* 3 (1982) 433–446.
- [87] M.S. Bhatti, R.K. Shah, Turbulent and transition flow convective heat transfer in ducts, in: S. Kakac, R.K. Shah, W. Aung (Eds.), *Handbook of Single-Phase Convective Heat Transfer*, Wiley-Interscience, New York, NY, USA, 1987.
- [88] I. Mudawar, Two-phase flow and heat transfer - lecture notes, Purdue University, West Lafayette, IN, USA, 2015.
- [89] S.M. Kim, I. Mudawar, Universal approach to predicting two-phase frictional pressure drop for mini/micro-channel saturated flow boiling, *Int. J. Heat Mass Transfer* 58 (2013) 718–734.
- [90] D.R.H. Beattie, P.B. Whalley, A simple two-phase frictional pressure drop calculation method, *Int. J. Multiphase Flow* 8 (1982) 83–87.
- [91] S.M. Zivi, Estimation of steady-state steam void-fraction by means of the principle of minimum entropy production, *J. Heat Transfer* 86 (1964) 247–252.
- [92] R.W. Lockhart, R.C. Martinelli, Proposed correlation of data for isothermal two-phase two component flow in pipes, *Chem. Eng. Prog.* 45 (1949) 39–48.
- [93] M. Al-Arabi, Turbulent heat transfer in the entrance region of a tube, *Heat Transfer Eng* 3 (1982) 76–83.
- [94] F.W. Dittus, L.M.K. Boelter, Heat transfer in automobile radiators of the tubular type, *Int. Commun. Heat Mass Transf.* 12 (1985) 3–22.
- [95] R.H.S. Winterton, Where did the Dittus and Boelter equation come from? *Int. J. Heat Mass Transfer* 41 (1998) 809–810.
- [96] V.S. Devahdhanush, S. Lee, I. Mudawar, Experimental investigation of subcooled flow boiling in annuli with reference to thermal management of ultra-fast electric vehicle charging cables, *Int. J. Heat Mass Transfer* (2020) under review.
- [97] F.D. Moles, J.F.G. Shaw, Boiling heat transfer to sub-cooled liquids under conditions of forced convection, *Trans. Inst. Chem. Eng.* 50 (1972) 76–84.
- [98] V.S. Devahdhanush, S. Lee, I. Mudawar, Consolidated theoretical/empirical predictive method for subcooled flow boiling in annuli with reference to thermal management of ultra-fast electric vehicle charging cables, *Int. J. Heat Mass Transfer* (2020) under review.
- [99] M.B. Bowers, I. Mudawar, Two-phase electronic cooling using mini-channel and micro-channel heat sinks - part 2. Flow rate and pressure drop constraints, *J. Electron. Packag.* 116 (1994) 298–305.
- [100] S.M. Kim, I. Mudawar, Review of two-phase critical flow models and investigation of the relationship between choking, premature CHF, and CHF in micro-channel heat sinks, *Int. J. Heat Mass Transfer* 87 (2015) 497–511.
- [101] G.B. Wallis, *One Dimensional Two-phase Flow*, 2nd ed., McGraw-Hill Inc., New York, NY, USA, 1969.

- [102] B. Hasanpour, M.S. Irandoost, M. Hassani, R. Kouhikamali, Numerical investigation of saturated upward flow boiling of water in a vertical tube using VOF model: effect of different boundary conditions 54 (2018) 1925–1936.
- [103] G. Son, V.K. Dhir, N. Ramanujapu, Dynamics and heat transfer associated with a single bubble during nucleate boiling on a horizontal surface, J. Heat Transfer 121 (1999) 623–631.
- [104] S. Hardt, F. Wondra, Evaporation model for interfacial flows based on a continuum-field representation of the source terms, J. Comput. Phys. 227 (2008) 5871–5895.
- [105] Q. Liu, W. Wang, B. Palm, A numerical study of the transition from slug to annular flow in micro-channel convective boiling, Appl. Therm. Eng. 112 (2017) 73–81.
- [106] K. Yokoi, D. Vadiello, J. Hinch, I. Hutchings, Numerical studies of the influence of the dynamic contact angle on a droplet impacting on a dry surface, Phys. Fluids 21 (2009) 072102.